10-17-2017

Fabrication and Characterization of Thermo-Optic Mach-Zehnder Silicon Modulator

Yeongho Park
Rose-Hulman Institute of Technology

Fabrication and Characterization of Thermo-Optic Mach-Zehnder Silicon Modulator

A Thesis

Submitted to the Faculty

of

Rose-Hulman Institute of Technology

By

Yeongho Park

In Partial Fulfillment of the Requirements for the Degree

of

Master of Science in Optical Engineering

October 2017

ROSE-HULMAN INSTITUTE OF TECHNOLOGY

Final Examination Report

Yeongho Park — Name

Optical Engineering — Graduate Major

Thesis Title: Fabrication and Characterization of Thermo-Optic Mach-Zehnder Modulator

DATE OF EXAM: October 17, 2017

EXAMINATION COMMITTEE:

	Thesis Advisory Committee	Department
Thesis Advisor:	Azad Siahmakoun	PHOE
	Michael McInerney	PHOE
	Edward Wheeler	ECE

PASSED X **FAILED**

ABSTRACT

Park, Yeongho

M.S.O.E

Rose-Hulman Institute of Technology

October 2017

Fabrication and Characterization of Thermo-Optic Mach Zehnder Silicon Modulators

Thesis Advisor: Dr. Azad Siahmakoun

This thesis focuses on the modeling, design, and fabrication of the Thermo-Optic Mach-Zehnder Modulator, which is one of the simple active devices in silicon photonics. The Mach-Zehnder interferometer (MZI) was formed as an optical path on a silicon on insulator (SOI) wafer of 2040$\pm$80 nm thick, and the thermo-optic effect was used to modulate the infrared light of 1553 nm wavelength by controlling the temperature of the one arm of the MZI.

To fabricate and understand the Si photonic device, the whole process from theory to the measurement setup is introduced. Additionally, all the fabrication details and some informative experiments which were performed during the fabrication are discussed for students who will study the more developed devices. The width of the designed waveguide is 4 μm, but the width of the fabricated waveguide is 3.0$\pm$0.2 μm due to the isotropic etching. For the lithography for both patterning waveguides and metal contacts, the AZ 5214 photoresist was used, and the details of the lithography was discussed. Furthermore, the lift-off method was performed and introduced to solve the over-etching problem. The

fabricated metal contacts can withstand up to 1.6W, and the electric power 0.3W is required to make Pi phase difference according to the simulation result by the simulation software Lumerical. The optical output of the device was not detected due to the huge losses from the sidewall roughness and the insertion loss, so it is discussed in the experimental measurement chapter.

ACKNOWLEDGEMENTS

I am grateful to my advisor Professor Azad Siahmakoun, who provided a great chance for a right direction and support throughout all the quarters I worked with him. He leads me to the goal despite challenges. All of my work was not possible without his support.

I would also like to express gratitude to Professor Wonjong Joo, my advisor in Seoultech. He gave me the chance to study at Rose-Hulman and, thought me to be a good student and person.

I would additionally like to thank technician Brian Fair, who helped me work in the clean room. He is the best colleague and teacher for all the fabrication process.

I would also like to thank Dr. Galen C. Duree, Dr. Granieri, and Pamela S. Hamilton in the Physics and Optical Engineering Department at the Rose-Hulman Institute of Technology for their support during my studies, and the opportunities that they have given to me.

Lastly, I would like to express my appreciation to my family in Korea for their blind faith and support.

TABLE OF CONTENTS

Contents

TABLE OF FIGURES

Figure Page

LIST OF TABLES

Table Page

1. Introduction

1.1. Background

In the last decade, there has been significant growth in the amount of data that people produce and consume. This demand for high performance is continually leading the development of the semiconductor industry. To overcome the limitation of 10 nm process and the bottleneck of the high data rate transmission, one workable solution is using photons to carry the information instead of electrons. Hence, silicon photonics is an attractive and promising technology in optoelectronic integration for computing, communication, and sensing [1], [2]. The key of silicon photonic technology is that multiple optical devices can be integrated on a single chip using the remarkably developed CMOS processing technology [3]. In recent years, the Photonics group at IBM research has developed an integrated optical interconnects to decrease the power consumption of IT systems [4]. Furthermore, Intel research has developed a prototype of 50 Gbps silicon photonic transmit module for chip to chip interconnects [5].

As shown in Figure 1.1, there are various components as a part of a system. The optical modulator is the simple and accurate active device to transfer the information signal. There are some primary electric field effects, such as the Pockels effect, the Kerr effect, and the Franz-keldysh effect. However, these effects are feeble due to the centrosymmetric crystal structure of silicon (Si) [6], [7]. Hence, the free carrier plasma dispersion or thermo-optic effect are the only available properties for modulation in silicon.

To obtain a high-speed modulator, it is more suitable to use the plasma dispersion effect (~GH) than the thermo-optic effect (~MHz). However, the plasma dispersion effect requires

more complicated fabrication steps to form the doping zone. As a first project of the fabrication of an active device, this thesis focuses on the study of the thermo-optic Mach-Zehnder Modulator (MZM).

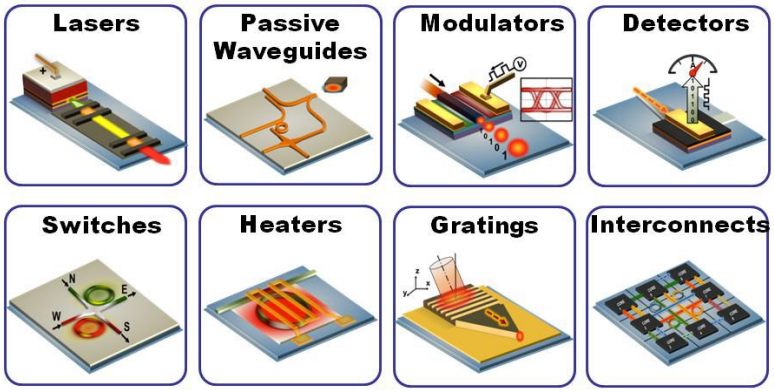

Figure 1.1 Main components in silicon photonic interconnects [8]

1.2. Silicon On Insulator (SOI)

Silicon photonics has an advantage due to its compatibility with CMOS technology so that the Si photonic devices can be fabricated without new fabrication techniques. This is the reason that Si photonics is very attractive area to the electronics industry. The refractive index of these silicon-based materials can be adjusted over a range between 1.45 (SiO_2) and 1.97 (SiO). It brings attractive advantage in terms of design and fabrication of waveguides [9].

Silicon is the most common material in the semiconductor technology and Photonics. In semiconductor devices, the silicon has a specific direction such as (111), (110), and (100) planes to maximize its properties. The crystal silicon wafers are formed by mostly Czochralski process [10]. Furthermore, there are additional processes to make a Silicon-On-Insulator (SOI) wafer, which is expensive. There are several different processes[11]

developed by big manufacturers, such as Soitec and Silicon Genesis Corporation. The SOI wafer which used for this thesis was made by Shin-Etsu Handotai (SEH). In Figure 1.2, the two different processes performed by SEH are represented.

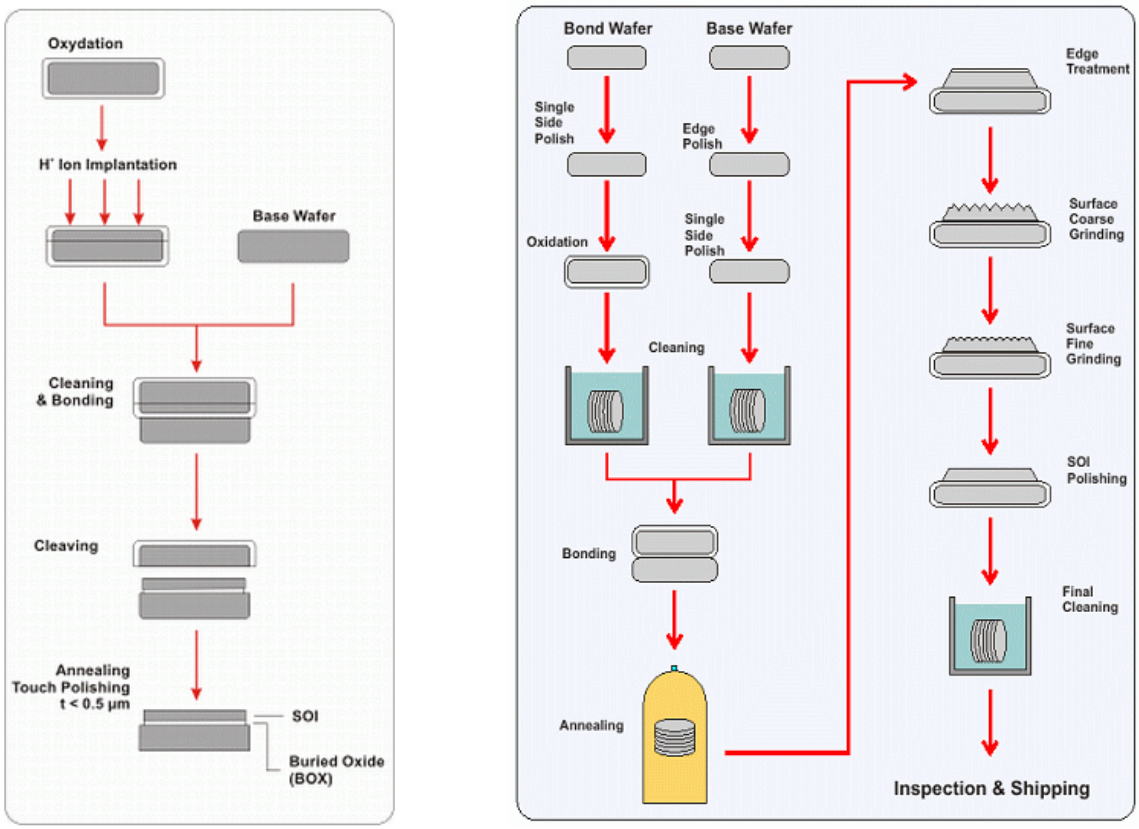

(a) unibond process (b) bonding and polishing process

Figure 1.2 (a) Unibond process is to fabricate the thin (<1µm) and (b) bonding and polishing process is to manufacture the thick (>1µm) SOI wafers The two processes are performed by SEH [12].

The process (a), called unibond, is a similar method with Separation by IMplantation of Oxygen (SIMOX) to form the exceptional top silicon layer uniformity (<±5%). However, this process is only possible for a thickness of 1000nm and below due to the limit of the

hydrogen implant. After cleaning and bonding, the wafer is separated from the bonded area at the limit of the hydrogen implant. Then, the SOI wafer is annealed and polished to have a smooth surface. On the other hand, the process (b), called bonding and polishing, produces the thick SOI wafers that are suitable for many semiconductor and MEMS applications. The required SOI wafer for the thesis is the thick one. Fabricating the thicker waveguide coupler will allow for obtaining optical signaling easily.

The crystal silicon is not essential for the silicon photonic devices because there are alternative materials, such as polycrystalline silicon and silicon nitride. Some experiments to demonstrate the poly-Si waveguide were performed. Even though the optical output coming through the poly-Si waveguide was not detected, the fabrication process will be introduced for future students. The p-Si waveguide must have more loss than the single crystal silicon waveguide because of the many grain boundaries. The grain boundary has mainly two kinds of loss mechanisms. The first is light absorption by the dangling bonds. The dangling bond is an unsatisfied valence, and is very reactive due to its lower energy level, as seen in Figure 1.3. The dangling bond is the defect state in the bandgap of silicon, and it allows two types of light absorption. Hence, photons lose their energy easily by the presence of the defect level between the conduction band and the valence band. The optical loss by the dangling bonds can be significantly reduced by the hydrogenation, which is called the hydrogen passivation [13].

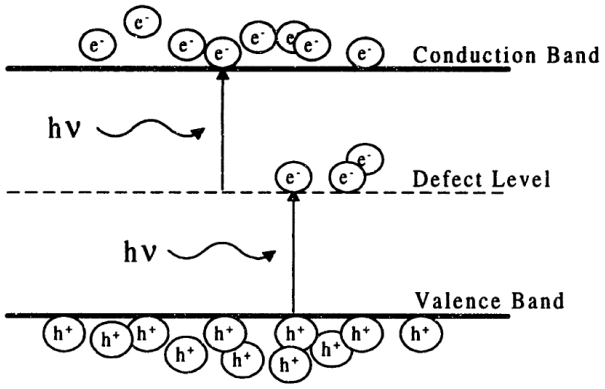

Figure 1.3 Two types of optical absorption [14]

The second loss mechanism is scattering at the grain boundary. The scattered light becomes higher order modes that interact more with waveguides, so it has more possibility to be absorbed or scattered again. As a result, the scattered light can be absorbed [15]. However, the loss by the grain boundary scattering can be reduced by heat treatment [16]. So, the treated polycrystalline silicon can be a core material, and fabricated in the clean room.

1.3. Objective

The objective of this thesis is to fabricate a thermo-optic effect modulator which was chosen to fabricate an active device without doping process as a first-step of fabrication. The goal is to minimize the transmission loss of the Si waveguide, and to modulate light at the standard communication wavelength of 1550 nm by the electric signal. This will permit the fabrication process to be retained for the next project, which will be the research of the plasma dispersion effect Mach-Zehnder Modulator (MZM).

2. Theory

In this chapter, three important concepts are introduced to understand the thermo-optic MZM. First, the waveguide theory is introduced as the most basic component in an integration circuit. The second is the Mach-Zehnder Interferometer (MZI), which is the most simple and powerful device in Si photonics. The last is the Thermo-Optic effect, which is the key of modulation for this device.

2.1. Waveguide

When light waves propagate through the two different mediums with some angle, the light rays are refracted in accordance with Snell's Law (1).

$$n_1 \sin\theta_1 = n_2 \sin\theta_2 \quad (1)$$

Where θ_1 is the incident angle and $\theta_2$is the angle of refraction as shown in the first case in Figure 2.1. The light can be entirely reflected in case that the refractive index is lower on the other side of the boundary and the incident angle is greater than the critical angle as illustrated in Figure 2.1. The angle of refraction approaches 90˚ as the incident angle increases. So, the critical angle $\boldsymbol{\theta_c}$ can be defined by using the angle 90˚and Snell's law, as represented in Eq. (2).

$$\theta_c = \sin^{-1}\frac{n_2}{n_1} \quad (2)$$

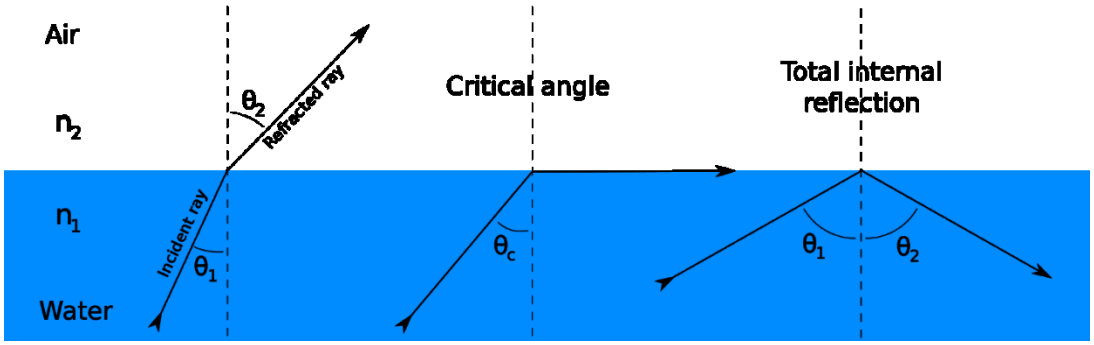

Figure 2.1 Light crossing the interface between two media of different refractive indexes represent different behavior depending on the incident angle [17].

For optical fibers and waveguides, the core material has a higher refractive index than the cladding material to induce the total internal reflection. Furthermore, the larger the index contrast leads, the smaller the critical angle, which allows more light to be guided.

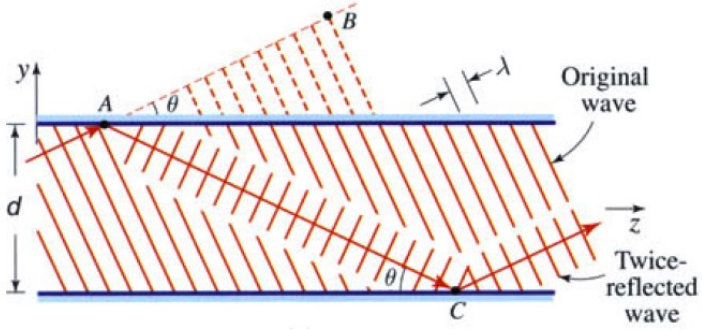

Figure 2.2 Condition of self-consistency: as a wave reflects twice it duplicates itself [18].

In silicon photonics circuits, the waveguide is the fundamental component to transfer the light information. The waveguide allows only a limited number of light waves, which is decided by the structure of the waveguide. The number is called mode, and a wave of a mode has self-consistency which means they repeat in phase and superimpose upon themselves.

The m_{th} (m = 1,2,3 ...) mode is divided by the each allowed incident angle θ_m. The first mode (m=1) experiences the least number of reflections due to the largest incident angle θ_1. This energetic mode is called the fundamental mode. Consequently, the higher modes have more losses by the more interactions with waveguides.

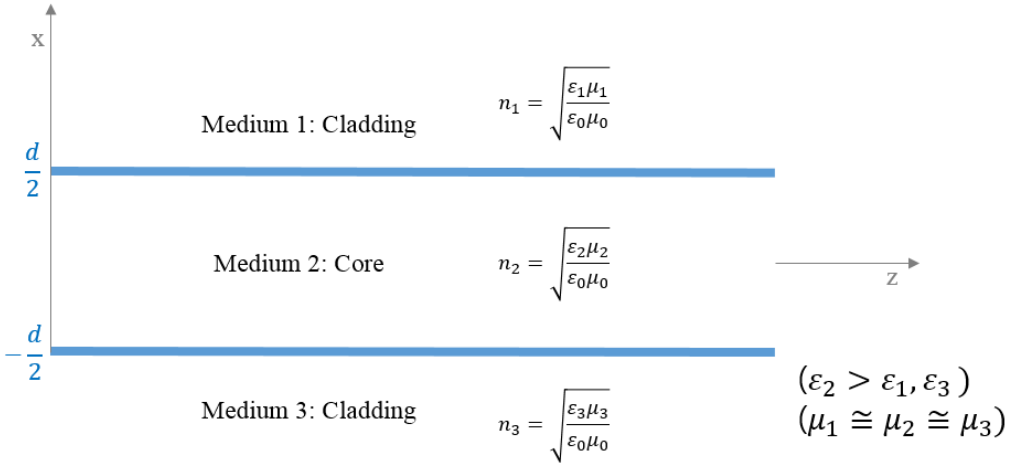

Figure 2.3 The slab waveguide: n is refractive index, ε is the permittivity, and μ is the permeability.

Consider a planar asymmetric waveguide described in Figure 2.3. The transverse electric (TE) field in the waveguide can be represented as

$$E_y(\mathrm{x},\mathrm{z}) = \begin{cases} A_1 e^{-\alpha_{1x}x} \cdot e^{-i\,k_z z} & x > {}^{d}/_{2} \\ A_2 \cos(k_{2x} + \psi) \cdot e^{-i\,k_z z} & |x| \le {}^{d}/_{2} \\ A_3 e^{-\alpha_{3x}x} \cdot e^{-i\,k_z z} & x > {}^{d}/_{2} \end{cases} \quad (3)$$

Where k_{2x} is the wavenumber in the x direction of the core, k_z is the propagation constant, d is the thickness of the core, and ψ(=0 or $\pi/2$) is the factor representing the even and odd modes. α is the dispersion relation. The dispersion equations are represented below

$$\alpha_{1x} = \sqrt{k_z^2 - \omega^2 \varepsilon_1 \mu_1} \qquad (4)$$
$$k_{2x} = \sqrt{\omega^2 \varepsilon_2 \mu_2 - k_z^2}$$
$$\alpha_{3x} = \sqrt{k_z^2 - \omega^2 \varepsilon_3 \mu_3}$$

Then, the magnetic field, H, is obtained directly from Maxwell's curl equation, $H_{z(x,z)} = \frac{i}{\omega\mu}\frac{\delta}{\delta x}E_y$(x,z)

$$H_z(\mathrm{x},\mathrm{z}) = \begin{cases} \dfrac{-i\alpha_{1x}}{\omega\mu} A_1 e^{-\alpha_{1x}x} \cdot e^{-i\,k_z z} & x > {}^{d}/_{2} \\ \dfrac{-ik_{2x}}{\omega\mu} A_2 \sin(k_{2x} + \psi) \cdot e^{-i\,k_z z} & |x| \le {}^{d}/_{2} \\ \dfrac{i\alpha_{3x}}{\omega\mu} A_3 e^{-\alpha_{3x}x} \cdot e^{-i\,k_z z} & x > {}^{d}/_{2} \end{cases} \qquad (5)$$

By applying the boundary condition at $\mathrm{x} = {}^{d}/_{2}$, the electric field and the magnetic field can be defined again as represented below

$$E_{tan} : A_1 e^{-\alpha_{1x}\,{}^{d}/_{2}} = A_2 \cos(k_{2x}\,{}^{d}/_{2} + \psi) \qquad (6)$$

$$H_{tan} : A_1 e^{-\alpha_{1x}\,{}^{d}/_{2}} = \frac{\mu_1 k_{2x}}{\mu_2 \alpha_{1x}} A_2 \sin(k_{2x}\,{}^{d}/_{2} + \psi) \qquad (7)$$

To simplify, equation (6) is divided by the equation (7) as below equation

$$\tan(k_{2x}\,{}^{d}/_{2} + \psi) = \frac{\mu_2 \alpha_{1x}}{\mu_1 k_{2x}} \qquad (8)$$

Similarly, the boundary condition at x=-d/2 is applied,

$$\tan(k_{2x}\ {}^{d}/_{2} - \psi) = \frac{\mu_2 \alpha_{3x}}{\mu_3 k_{2x}} \tag{9}$$

The equation (8), and (9) are represented again by using the periodic property of tangent.

$$k_{2x}\ {}^{d}/_{2} + \psi = \frac{1}{2}\Phi_1^{TE} \pm n\pi \qquad (n = 0,1,2 \ldots) \tag{10}$$

$$k_{2x}\ {}^{d}/_{2} - \psi = \frac{1}{2}\Phi_3^{TE} \pm m\pi \qquad (m = 0,1,2 \ldots) \tag{11}$$

Where, $\Phi_1^{TE} = 2\tan^{-1}(\frac{\mu_2 \alpha_{1x}}{\mu_1 k_{2x}})$, $\Phi_3^{TE} = 2\tan^{-1}(\frac{\mu_2 \alpha_{3x}}{\mu_3 k_{2x}})$.

By combining both equations (10), and (11), a simple equation is derived below,

$$k_{2x}\, d - \Phi_1^{TE} - \Phi_3^{TE} = 2p\pi \qquad (p = 0,1,2 \ldots) \tag{12}$$

$$(\boldsymbol{n \pm m = p}, \qquad \boldsymbol{m \pm n = p})$$

From the equation (12), the b-ν equation (16) is derived by applying the below functions.

$$\nu = k_0 d\sqrt{{(\varepsilon_2 - \varepsilon_3)}/{\varepsilon_0}} \tag{13}$$

$$\mathrm{b} = \frac{\varepsilon_{eff} - \varepsilon_3}{\varepsilon_2 - \varepsilon_3} \tag{14}$$

$$a = \frac{\varepsilon_3 - \varepsilon_1}{\varepsilon_2 - \varepsilon_3} \tag{15}$$

Where the wavenumber $k_0 = \omega\sqrt{\mu_0 \varepsilon_0}$, and the effective permittivity $\varepsilon_{eff} = \varepsilon_2 - \frac{k_{2x}^2}{\mu\omega^2}$. The ν is a parameter that determines the cutoff condition for mode propagation in the

waveguide. It is called the normalized frequency or ν parameter. The b parameter is a normalized propagation constant shown as a function of ν. The *a* represents the degree of asymmetry in the waveguide. By applying the functions (13),(14), and (15) to the equation (12), the b-ν equation is derived as;

$$\nu\sqrt{1-b} = p\pi + \tan^{-1}\sqrt{b/(1-b)} + \tan^{-1}\sqrt{(b+a)/(1-b)} \qquad (16)$$

From the equation (16), the number of the confined modes can be found as shown in Figure 2.4.

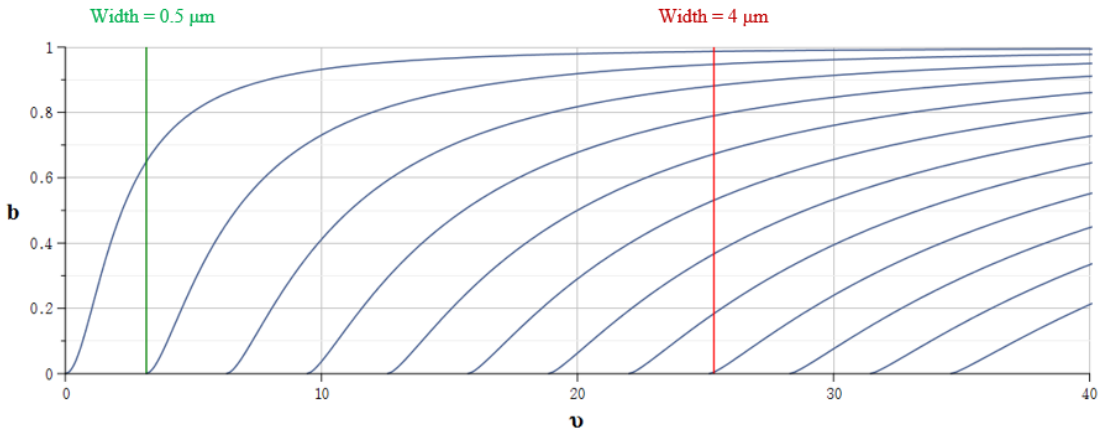

Figure 2.4 The normalized frequency b versus the normalized propagation constant *v* of a silicon waveguide. The vertical lines are the size factor of the waveguide. The vertical lines are from the equation (13) and all the constants and each dimension d are substituted in the equation.

The core material is silicon (n_2=3.5), and cladding material is silicon dioxide (n_1=n_3=1.5) as same as the designed waveguide. The dimension of the normal single mode waveguide is 500×220 nm (width×height), whereas the dimension of the width of the designed

waveguide is 4μm. The reasons for the large dimension are to overcome the limitation of the fabrication techniques and to get more light into the edge coupler from the optical fiber. The large dimension of the waveguide accepts the large incident angle, and the wide incident angle makes the multiple modes. Each dimension allows the different number of modes corresponding with the number of the intersections between each vertical line and the function b. According to this theory, the normal single mode waveguide has only the fundamental mode, and the width of the designed waveguide allows the nine TE modes as shown below Table 2.1.

Table 2.1 The TE modes in the designed waveguide.

Mode #	Electric field distribution	Modal fields
0 (Fundamental)	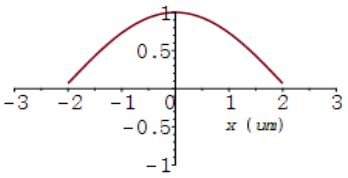	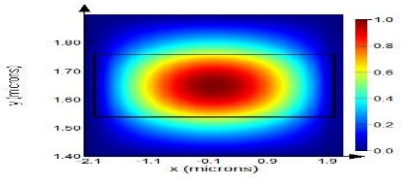
1	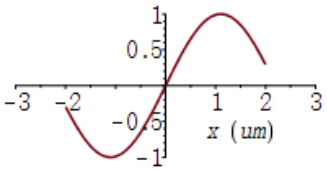	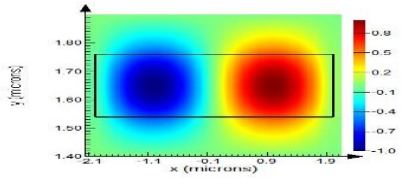
2	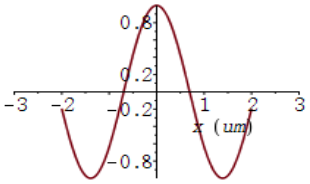	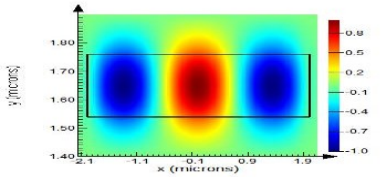
3	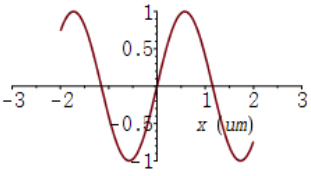	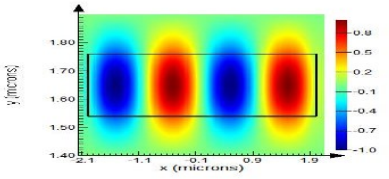

4	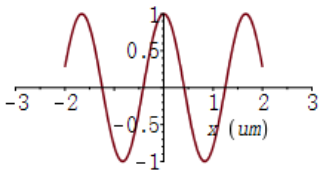 1 0.5 -3 -2 1 2 3 -0.5 -1 x (um)	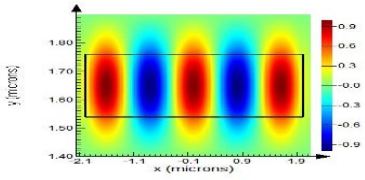 y (microns) 1.80 1.70 1.60 1.50 1.40 2.1 1.1 0.1 0.9 1.9 x (microns) 0.9 0.6 0.3 -0.0 -0.3 -0.6 -0.9
5	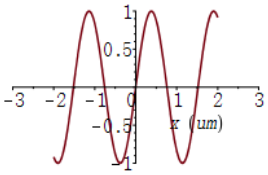 1 0.5 -3 -2 -1 0 1 2 3 -0.5 -1 x (um)	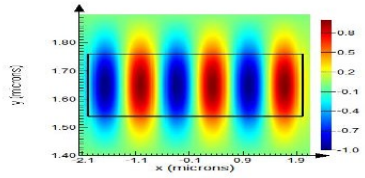 y (microns) 1.80 1.70 1.60 1.50 1.40 2.1 1.1 0.1 0.9 1.9 x (microns) 0.8 0.5 0.2 -0.1 -0.4 -0.7 -1.0
6	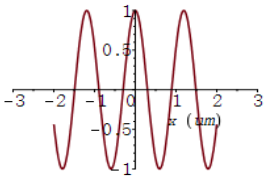 1 0.5 -3 -2 -1 0 1 2 3 -0.5 -1 x (um)	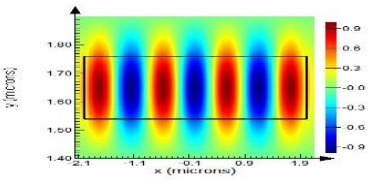 y (microns) 1.80 1.70 1.60 1.50 1.40 2.1 1.1 0.1 0.9 1.9 x (microns) 0.9 0.6 0.3 -0.0 -0.3 -0.6 -0.9
7	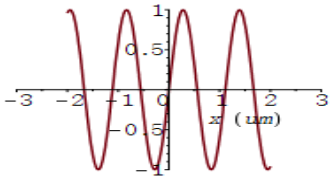 1 0.5 -3 -2 -1 0 1 2 3 -0.5 -1 x (um)	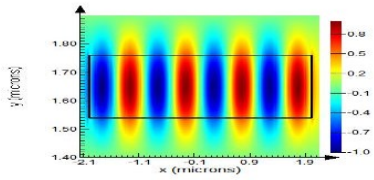 y (microns) 1.80 1.70 1.60 1.50 1.40 2.1 1.1 0.1 0.9 1.9 x (microns) 0.8 0.5 0.2 -0.1 -0.4 -0.7 -1.0
8	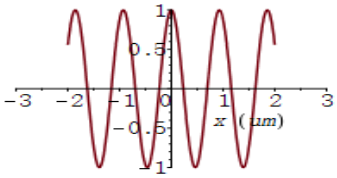 1 0.5 -3 -2 -1 0 1 2 3 -0.5 -1 x (um)	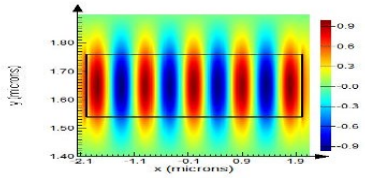 y (microns) 1.80 1.70 1.60 1.50 1.40 2.1 1.1 0.1 0.9 1.9 x (microns) 0.9 0.6 0.3 -0.0 -0.3 -0.6 -0.9

The modes mentioned above are only TE modes, and the height of the waveguide was assumed as 220 nm to consider the effect of the waveguide width. As seen in Table 2.1, the higher modes interact with the medium, and reflect to the interface more than the fundamental mode does because the fundamental mode has the smallest incident angle. Considering that the height of the waveguide allows multi modes, the total number of the modes will be increased, and the group index will be decreased more. Hence, the waveguide having multi modes is not proper to transfer the high-frequency information through long distance. However, it was the unavoidable choice for this experiment as mentioned before. There are normally two types of waveguides, strip waveguide and rib waveguide, which are illustrated in Figure 2.5. The rib waveguide is popular in designing active devices such as modulators because the slab region of the rib waveguide is suitable for the doping [19]. The SiO_2 layer under the Si waveguide causes high refractive index contrast between silicon (n=3.467) and SiO_2 (n=1.444), so it can have a high confinement. In Figure 2.5, the top cladding is not expressed, but it will be fabricated to protect the devices and to form the metal contact above the waveguides [20]

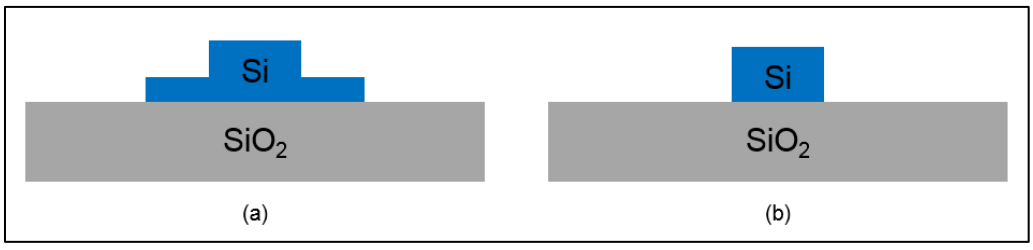

Figure 2.5 (a) rib waveguide, also known as ridge waveguide, and (b) strip waveguide, also known as channel waveguides, or photonic wires.

2.2. Mach-Zehnder Interferometer

The Mach-Zehnder Interferometer (MZI) is an optical device that works according to the Interferometer effect: an input signal is divided between two paths; a given phase change is applied to the signals in each path; and finally, both signals are recombined at the output as shown in Figure 2.6.

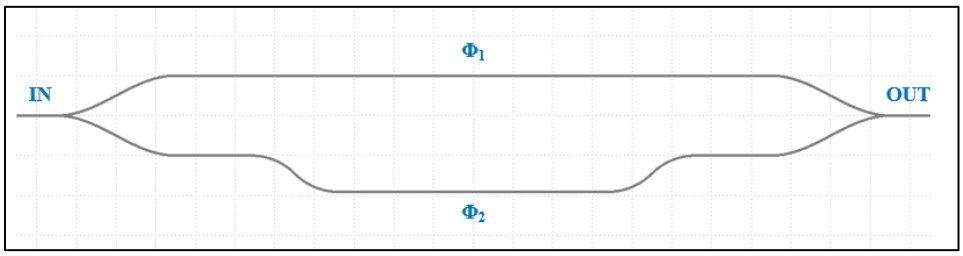

Figure 2.6 Schematic of Mach-Zehnder Interferometer

Where Φ_1 and Φ_2 are the phases of two arms. If the interferometer is analyzed as a system, it is possible to find a transfer function, T, given by equation (17)

$$T = \cos^2(\Delta\Phi) = \cos^2\left(\frac{2\pi}{\lambda}(n_1L_1 - n_2L_2)\right) \tag{17}$$

Where $\Delta\Phi$ is the phase difference between the two branches, $n_{1,2}$ are the effective refractive indexes of each arm, and $L_{1,2}$ is the length of the two arm. The main wavelength, λ of input light for this study is 1553 nm. It is necessary to note that this transfer function works in an ideal case, where system losses and anisotropies are not considered.

In this case, the parameter $\Delta\Phi$ is the phase difference between both optical paths, i.e. it is a function of the physical length and the refractive index of each branch. Because the transfer function is a periodic function, we are interested in analyzing the cases in which it becomes

maximized:

$$T = 1 \rightarrow \Delta\Phi = m\pi \; with \; m \in \mathbb{N} \tag{18}$$

To use a MZI as a modulator, the effective refractive index of the waveguide can be controlled by changing environmental conditions such as pressure, temperature, or electric-field flux. Thus, two types of modulators exist to control an optical signal: electro-optic MZM, and thermo-optic MZM.

$$\Delta\Phi = \frac{2\pi}{\lambda} \Delta n_{eff} \, \Delta L \tag{19}$$

Where Δn_{eff} is the difference between the two effective refractive indexes, and ΔL is the length difference between the two arms. The effective refractive indexes of the both arms are same, but it will be different after changing the temperature of one arm. This is called thermo-optic effect which will be explained in the next chapter.

2.3. Thermo-Optic effect

Thermo-Optic effect is a change in the optical properties of a material in response to the temperature. When the temperature is increased by applying electric power, the bandgap energy of the silicon is decreased as shown in Figure 2.7. Hence, the photon can be absorbed into the electron in the valence band more easily due to the reduced bandgap. As a result, the attenuation is increased and the refractive index is also increased. This is how the temperature effects the refractive index of the waveguide and why each material has a different degree of the thermo-optic effect.

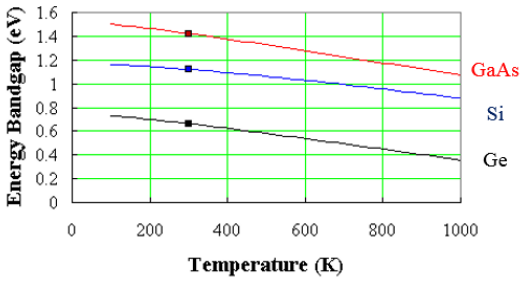

Figure 2.7 Bandgap energy variation of semiconductor materials by the temperature increase

Thermo-Optic Silicon MZM can achieve differences in the refractive index of 10^{-4} by controlling the temperature. In this case, the physics behind the problem are much simpler if we ignore the effects of thermal displacement and expansion. The simplest model for a change in the refractive index is given by the equation:

$$n = n_0 + \frac{dn}{dT}\Delta T \tag{20}$$

Where n_0 is the given refractive index of the material, $\frac{dn}{dT}$ is the thermo-optic coefficient and ΔT is the temperature difference between two points. Since the thermo-optic coefficient is different for each material, the factor that we need to analyze is $\frac{dn}{dT}$. These values can be obtained numerically for the waveguide material, silicon, in this study.

$$\frac{dn}{dT} = 1.87 \times 10^{-4} K^{-1} \tag{21}$$

The Thermo-Optic effect is one of the main effect of this project. The effective refractive index of Si waveguide is changed by controlling the temperature of the heat pad.

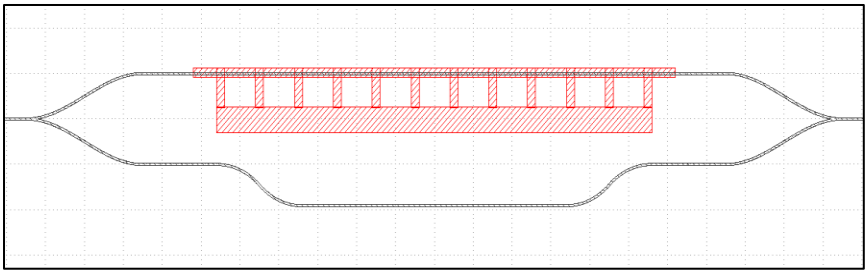

Figure 2.8 The designed Thermo-Optic MZM. The red boxes are heat pads to make temperature change by applying voltage.

The dimension of the Si waveguide is 4×0.22 μm (width×height). The length of sensing arm, L_1, is 650 μm, and the length of the reference arm, L_2, is 680 μm. The heat pad covers the length of 620 μm of sensing arm. The interferometer was designed to have the lowest intensity at the 1553nm wavelength when there is no heat. The transfer function (= I_o/I_i) is seen below (22).

$$T = \frac{1}{2}\left[1 + cos\left(\frac{2\pi n}{\lambda}\Delta L - \frac{2\pi\left(\frac{dn}{dT}\Delta T\right)}{\lambda}L_1\right)\right] \quad (22)$$

Where n is the effective refractive index of Si waveguide. The output of the modulator is changed by the temperature variation as shown below Figure 2.9.

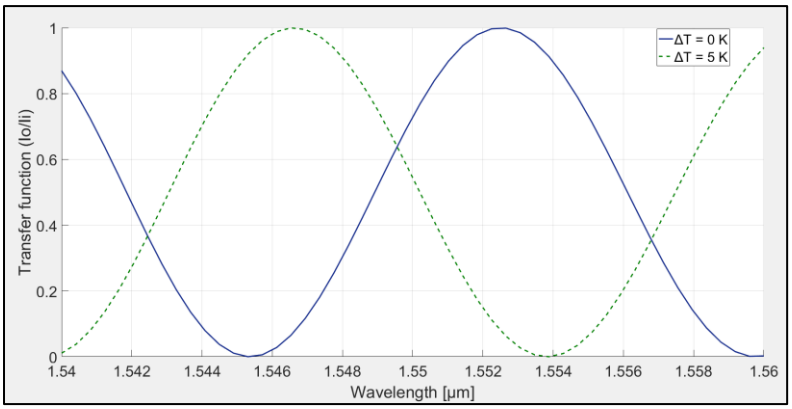

Figure 2.9 The transfer function of the modulator with temperature change. n_{eff} is 3.24345 and ΔL is 30 μm.

In practice, switching frequencies in the order of MHz have been achieved with Thermo-optic MZM, while frequencies of ~10 GHz have been achieved with PIN MZM [9].

Figure 2.10 shows the numerical results of the effective index's dependence on temperature. This simulation was made ignoring dispersion effects or any loss by Joule effect. The figure displays the values for 3 geometries: 500×220 nm strip waveguide (black), 500×220 nm with 90 nm rib waveguide (red), and the multimodal 4000×220 nm strip waveguide used in this design (blue).

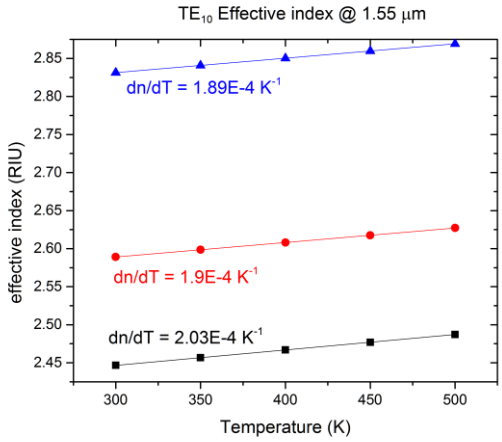

Figure 2.10 Effective index dependence on temperature for the TE10 mode on the given waveguides.

3. Simulation

Simulations were performed by the following Lumerical software: Mode Solutions, Lumerical FDTD, and Lumerical Device. The software packages each have their own purpose. The Mode Solutions is used to obtain the optical properties, such as effective refractive index and mode of the propagating light. The Lumerical FDTD was used to check the transmission of each device. The Lumerical Device gives information about doping and thermal transfer of the active device. The advantage of these software packages is that they can interface with each other. So, the device blocks can be formed and simulated for its heat transfer by the Lumerical Device, and then the heat transfer information of the block can be exported to be used in the Mode Solutions to see its optical properties. These interconnections seem complicated, but actually are very simple and powerful software for Si photonics.

3.1. Waveguides

The common dimension of the waveguide to form single mode is 500×220 nm. However, the dimension of the designed waveguide is 4,000×500 nm due to the limitation of lithography resolution and to simplify the experiment. Even though the resolution is known as 1 μm, it is not easy to get 1 μm width using the UV lithography and isotropic etching process.

Using a simulation software makes it simple to get optical properties of the designed waveguide as shown in Figure 3.1.

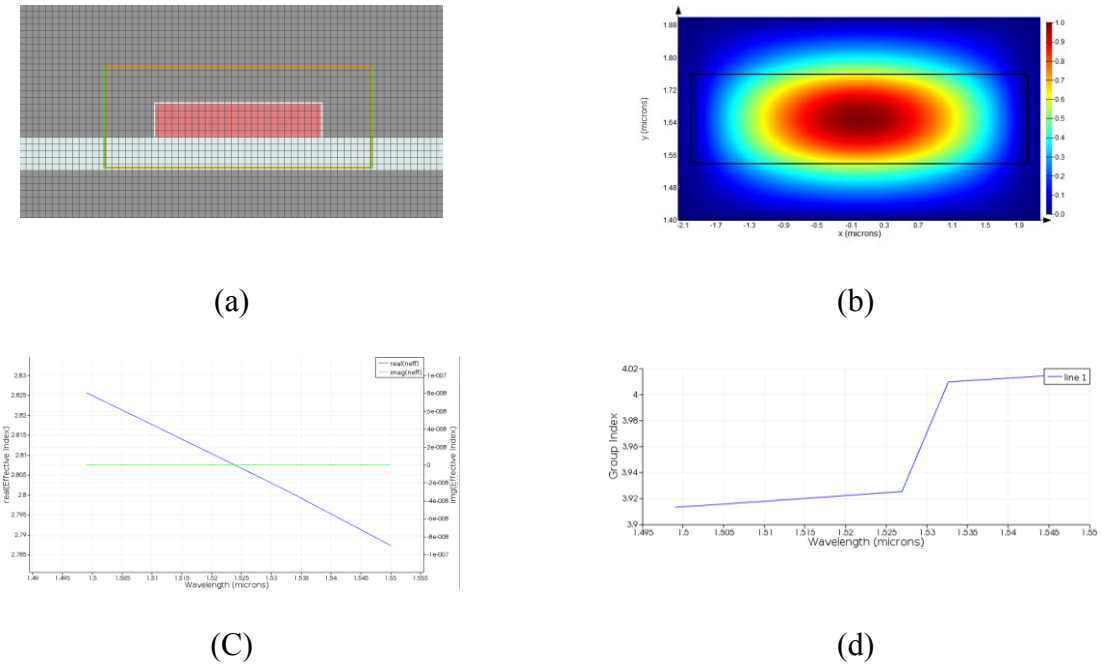

Figure 3.1 (a) Designed waveguide, and simulation solver (orange-green box) and (b) The fundamental mode profile in MODE Solutions. As the dimension is 4×0.5 µm, there are 45 modes, but only the fundamental mode is considered for calculations or other simulations. (c) The effective refractive index of the fundamental mode is 2.79 at 1553nm wavelength. (d) The group index of the fundamental mode as a function of wavelength.

3.2. Edge Coupler

The light is delivered by the optical fiber, and the diameter of the fiber core is 9 µm. In contrast, the dimension of the designed waveguide is 4×0.5 µm which is almost 32 times smaller than that of the single mode fiber area [20]. Hence, the components to be between the fiber and the waveguide are required to transfer the light with minimum loss. Normally, there are two ways to put the light from the fiber into the device shown in Figure 3.1. The first method is grating coupler which requires high-resolution lithography. It makes

taking measurement easy, even if it requires the high-resolution fabrication process such as the e-beam lithography. As mentioned in the previous chapter, the limitation of UV light resolution allows only the fabrication of the edge coupler. Even though it is difficult to cut the wafer and to test the device, the fabrication process of the edge coupler needs only one of the same steps as the waveguide fabrication.

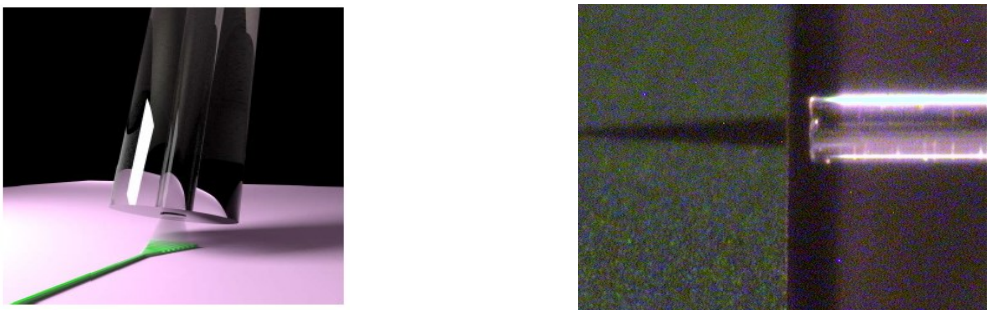

(a) (b)

Figure 3.2 (a) Grating coupler [21] and (b) Edge coupler with the optical fibers

In 1977, Milton and Burns proposed a simple design direction for a symmetric taper [22]. The designed taper was followed the design direction shown in the equation below.

$$\theta < \frac{\lambda_0}{2Wn_{eff}} \tag{23}$$

Where θ is the half angle of the taper at the point z, λ_0 is the wavelength in vacuum, n_{eff} is the effective refractive index, and W is the full width of the taper at point z as represented in Figure 3.3.

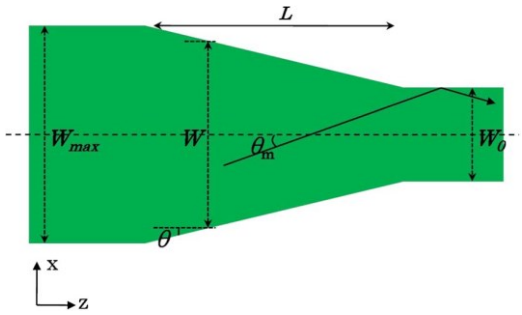

Figure 3.3 Schematic of a linear taper [23]

The equation (23) can be represented more simply by inserting a constant α as shown below in equation (24).

$$\theta = \alpha \frac{\lambda_0}{2Wn_{eff}} \tag{24}$$

According to the reference [23], α should be less than 1.4 to get high coupling efficiency in case of a single mode waveguide. For the multi-mode, α can be greater the 1.4. Following this simple rule, the taper was designed and simulated to consider the dimension of the fiber and each cell. The dimensions of the designed taper are W_{max}=12μm, W_0=4μm, and L=160μm as shown in Figure 3.4.

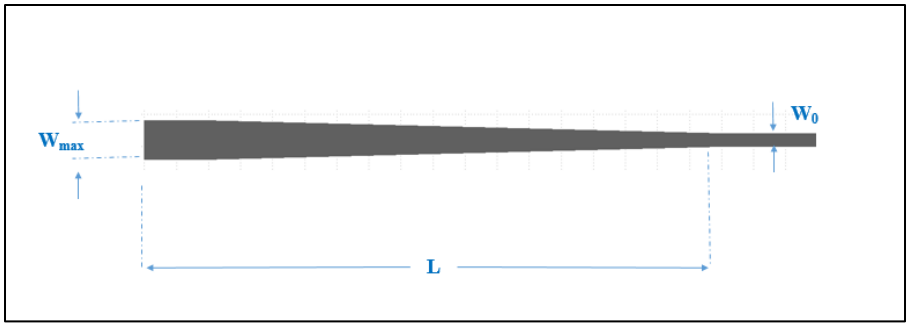

Figure 3.4 The designed edge coupler by the K-layout. W_{max}=12μm, W_0=4μm, and L=160μm.

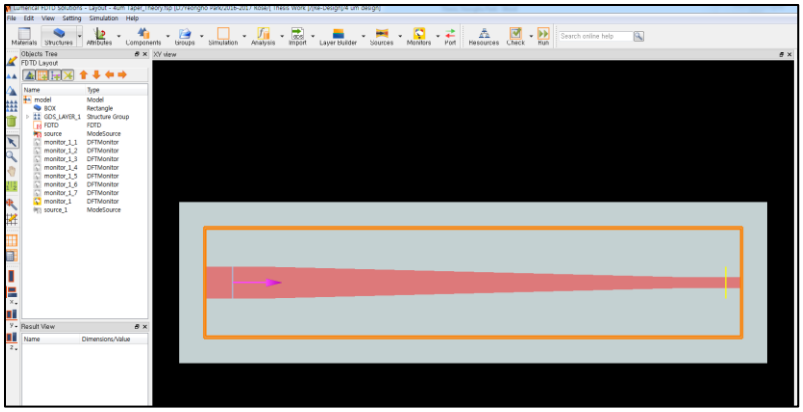

Figure 3.5 The edge coupler simulation in Lumerical MODE Solutions.

The result of the taper simulation is shown in Figure 3.6. The light source for this simulation is 1553nm with the bandwidth of 2 nm which is the same as the light source used in the experiment. The insertion loss between the optical fiber and the facet of the edge coupler was not considered. The transmission of the edge coupler is 98.7%. The reason for the high transmission is that the only loss is from the tapered structure of the edge coupler.

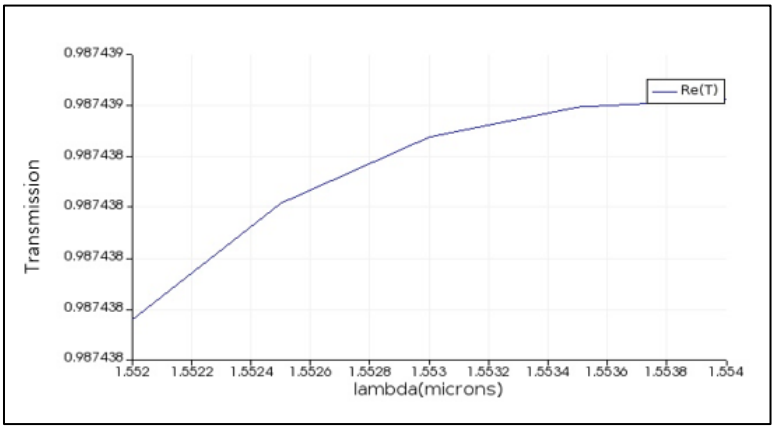

Figure 3.6 Simulation result; Transmission of the edge coupler.

3.3. Y-Branch

The next component of the MZM is a beam splitter/combiner. Normally in photonics, there are two kinds of components to split the light from one waveguide or to combine light from two waveguides into one [20]. The first one is directional coupler which consists of two parallel waveguides. The coupling coefficient is decided by the length of the two waveguides and the gap between them as shown in Figure 3.7. The common coupler gap is 200nm for fabrication and proper coupler length. This is the reason why the coupler could not be adapted for the MZM. This project would be performed in Rose-Hulman clean room where there is no E-beam lithography.

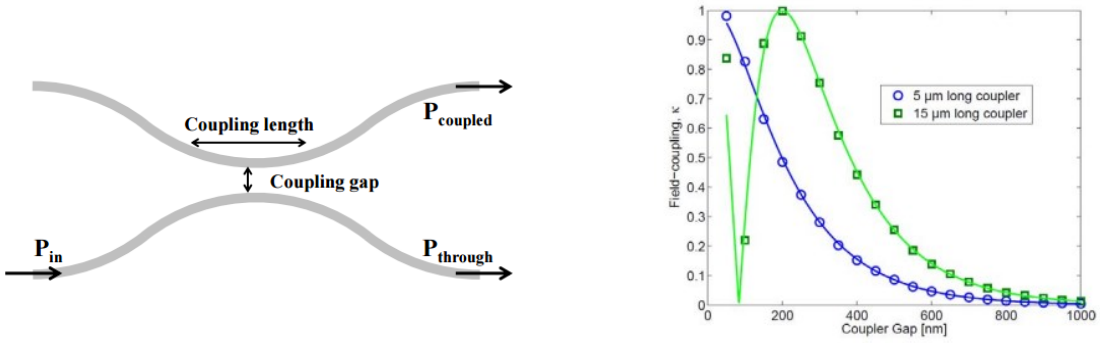

(a) (b)

Figure 3.7 (a) schematic of directional coupler, and (b) Coupling coefficient versus coupler gap at wavelength 1550nm [24]

Compare to the directional coupler, Y-branch is straightforward to understand as seen in Figure 3.8. It consists of two symmetrical arms with curvature to connect a straight waveguide smoothly [25]. The shape of splitter and combiner are identical. Hence, the same equations (25, 26) are applied to make a different system.

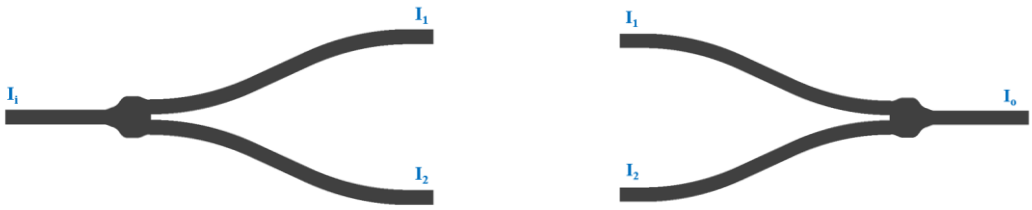

(a) (b)

Figure 3.8 Schematic of (a) Y-branch splitter, and (b) Y-branch combiner [26]

$$I_1 = I_2 = \frac{I_i}{2} \tag{25}$$

$$E_1 = E_2 = \frac{E_i}{\sqrt{2}} \tag{26}$$

So, theoretically, the splitter can split the input light 50/50% into each branch. However, the combiner has two different cases. In the first case, the phase of two arms are identical. The two coherent beams of light can combine and increase the intensity, $I_1 + I_2 = I_o$.

In the second case, the two beam of light have different phase such as the two beams are from different arm length. Hence, they cannot interfere each other constructively, making the reduced intensity, $I_1 + I_2 < I_0$ due to the destructive interference.

Besides, the Y-branches must have an excess loss in a real device. Therefore, the simulation is important to optimize the geometry of the Y-branch. The optimized insertion loss in the reference [27] is less than 0.3dB.

The designed Y-branch is shown in Figure 3.9. The length, L, is 120 μm and the gap, g, is 40 μm. This dimension is the result of considering the position of the metal contacts and the

device test after fabrication.

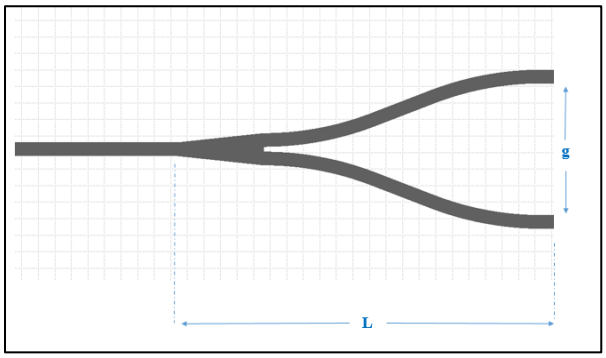

Figure 3.9 The designed Y-branch by K-Layout. L= 120 µm, g= 40 µm and the width of the waveguide= 4 µm

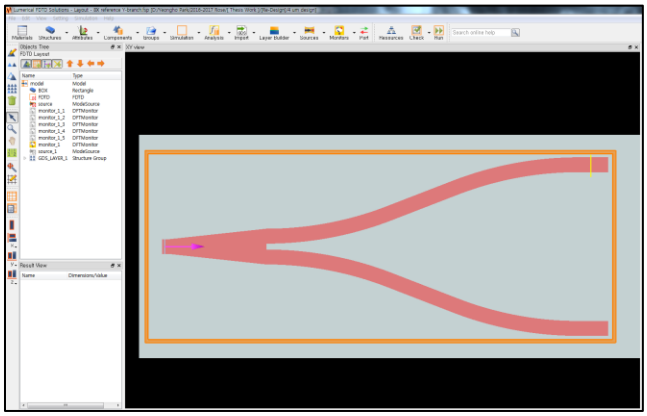

Figure 3.10 The simulation of the Y-branch splitter using the Lumerical FDTD solutions

In Figure 3.10, the white rectangle is the silicon dioxide layer, and the orange box is a simulation monitor. The light source is placed in the head of the Y-branch, and the transmission monitor, shown as a yellow stick, is placed on the end of the one arm. The simulation result is shown in Figure 3.11. The transmission is less than the theoretical value 50% because the simulation software considered the mode expansion and the loss from the

structure.

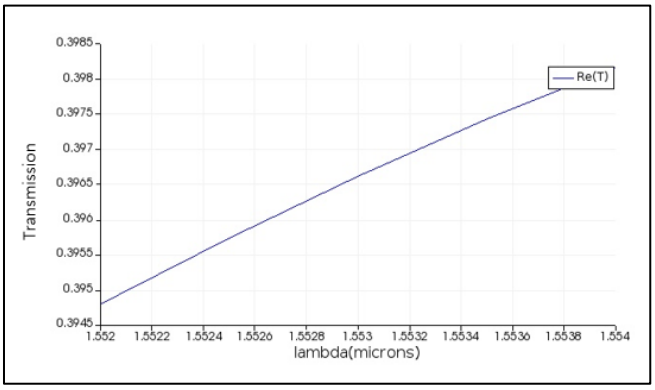

Figure 3.11 Simulation result of the Y-branch splitter; transmission vs. wavelength. The center wavelength of the laser is 1553 nm and the bandwidth is 2 nm.

As mentioned, the Y-branch combiner has a different efficiency even though it has same structure as the Y-branch splitter. Therefore, the combiner was simulated with the same condition, but there are two light sources from each arm as shown in Figure 3.12. The two light source are placed for the in-phase condition, and the transmission monitor is placed on the end of the combiner.

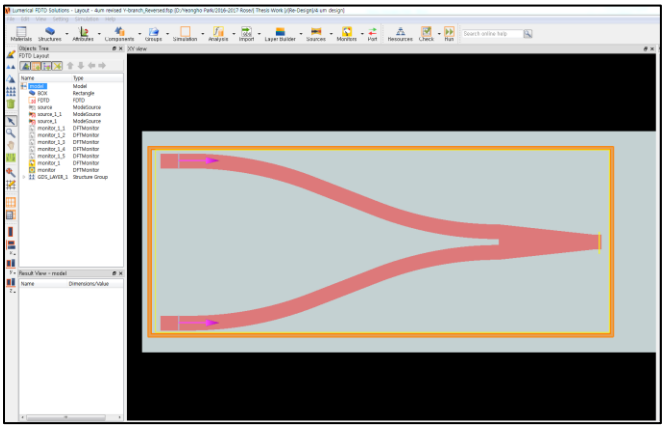

Figure 3.12 The simulation of the Y-branch combiner

As shown in Figure 3.13, the transmission of the combiner is about 47%, even though the light source from the two arms is in-phase. Theoretically, the transmission of the combiner

with two in-phase inputs should approach 100%. However, there are unavoidable losses from the multimode waveguide, bend, and the structure of the Y-branch.

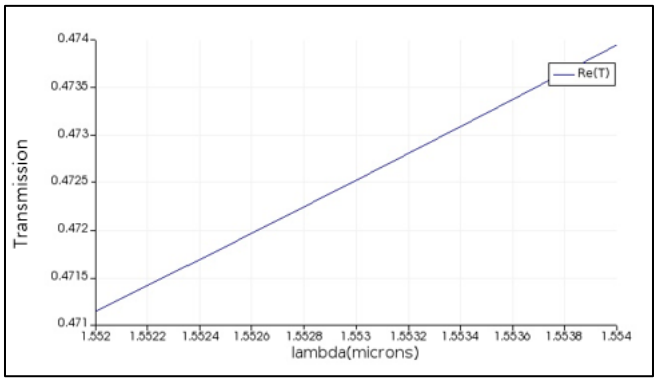

Figure 3.13 Simulation result of the combiner; transmission vs. wavelength. The center wavelength of the laser is 1553 nm and the bandwidth is 2 nm.

3.4. Thermo-Optic Mach-Zehnder Modulator

The main component of the thermo-optic Mach-Zehnder Modulator (MZM) is the sensing arm with the heat pad. As mentioned in previous chapters, the MZM consists of two Y-branches, a reference arm, a sensing arm, and a heating pad as shown in Figure 2.8. By applying voltage, the heat pad can generate the temperature variation which causes the effective index change. To check the variation, the heat transfer simulation was performed by using Lumerical DEVICE as shown below.

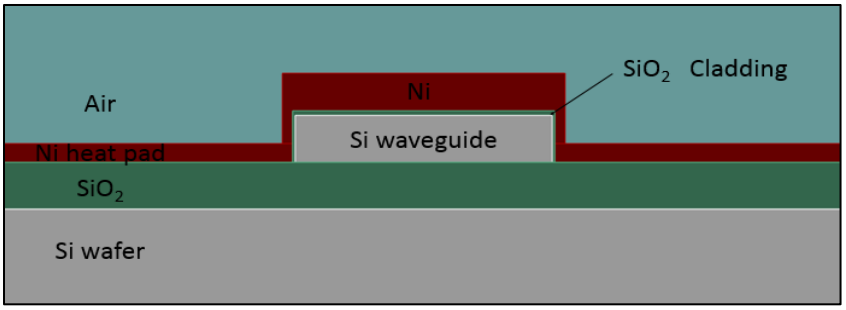

Figure 3.14 Schematic of the Thermo-Optic MZM in Lumerical DEVICE.

Table 3.1 The heat transfer and temperature at each electrical power. In each figure, the only SiO_2 layer and Si waveguide are seen, and the scale bar unit is Temperature K.

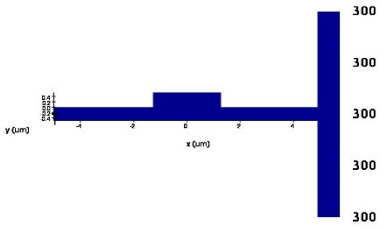	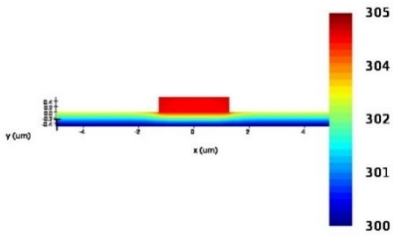
0 W	0.2 W
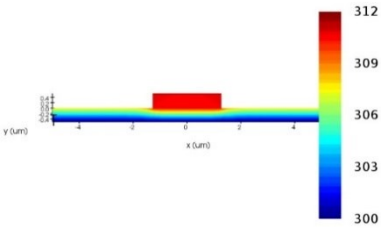	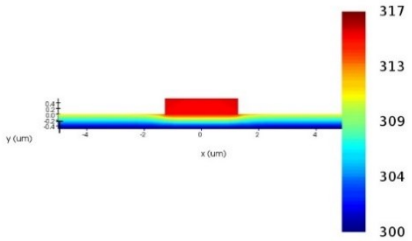
0.5 W	0.7 W
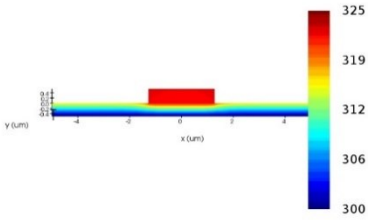	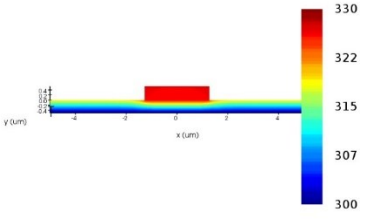

1.0 W	1.2 W
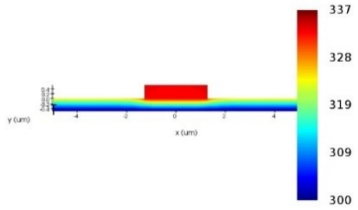	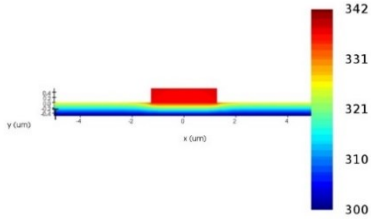
1.5 W	1.7 W

In the heat transfer simulation, the heat pad is not represented, but cladding, waveguide, and BOX are seen with its temperature change. Through this simulation using Lumerical DEVICE, the relationship between electric power and temperature of each material is explained. To know the effective refractive index change, the heat transfer data needs to be exported and imported to the Lumerical MODE Solutions. The final simulation result is shown in Figure 3.15.

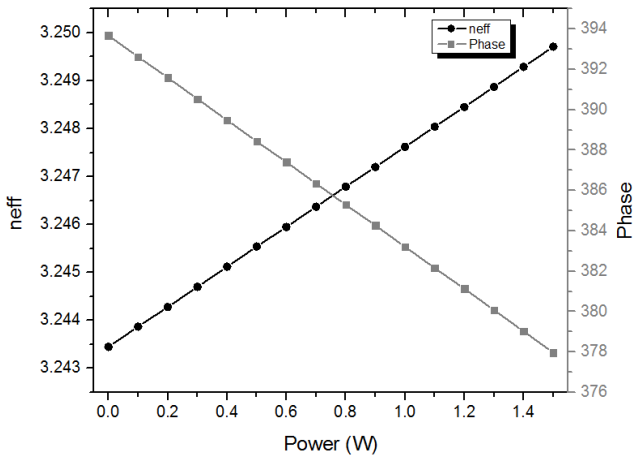

Figure 3.15 Effective refractive index and phase versus power. λ_0 is 1553nm and ΔL is 30 μm.

Using the simulation data, the transfer function was calculated as shown in Figure 3.16.

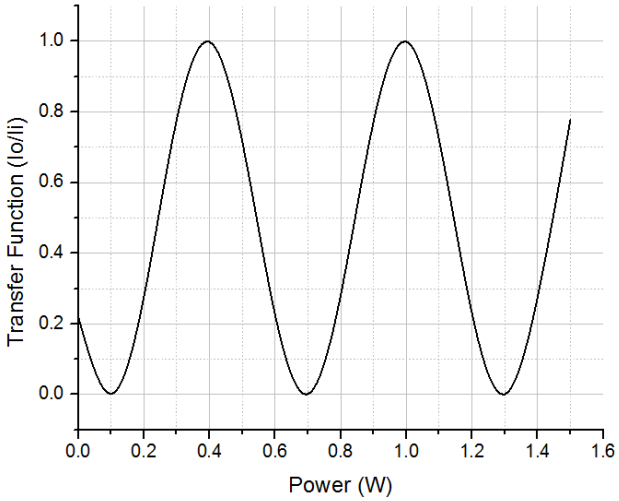

Figure 3.16 Transfer function of the thermo-optic silicon MZM

4. Fabrication

4.1. Fabrication process flow

The fabrication process was planned to start from the wet oxidation and the silicon deposition to form the polycrystalline silicon on the box layer. However, there were some problems to fabricate the low loss p-Si layer as a waveguide core material. The incomplete experiment is introduced in the next chapter as one of the failed experiments. To get the lossless waveguide, a commercial SOI wafer was used as mentioned in the previous chapter. The whole fabrication process is represented below Table 4.1.

Table 4.1: The fabrication process flow

	Process	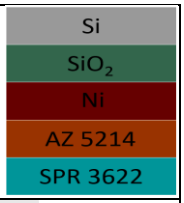
1	RCA clean	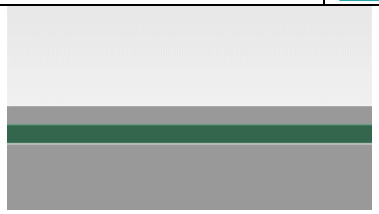
2	Lithography; AZ5214	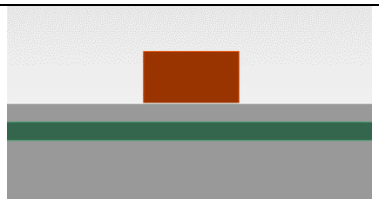
3	Si Etching; XeF_2	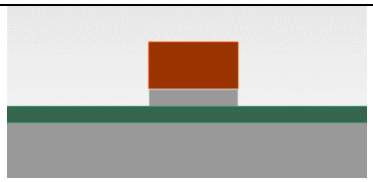

4	P.R remove; Plasma Asher	
5	SiO_2 Deposition; e-beam evaporator	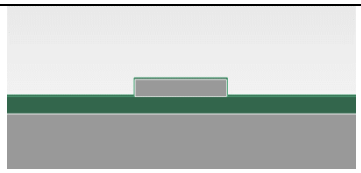
6	Ni Deposition; e-beam evaporator	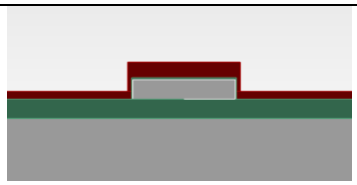
7	Lithography; SRP3622	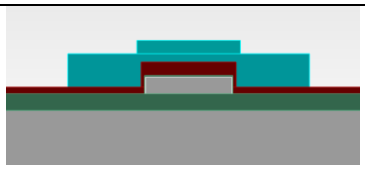
8	Ni Etching; Nitric & Acetic acid	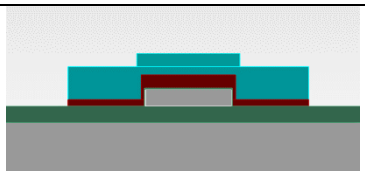
9	Wafer cutting; Sawing machine	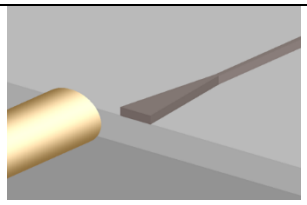
10	Cleaning using acetone	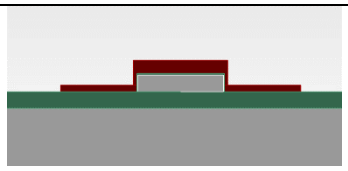

4.1.1. SOI wafer

As mentioned in the introduction chapter, the commercial SOI wafer shown in Figure 4.1 was used for this fabrication. The SOI wafer has the silicon <111> layer of 2.2 μm on the box layer of 1.1 μm. Even if the details on the wafer box shows the thickness of each layer, it was double-checked by the Filmetrics which is a thin film measurement system. Because knowing the uniformity is quite important during the etching process.

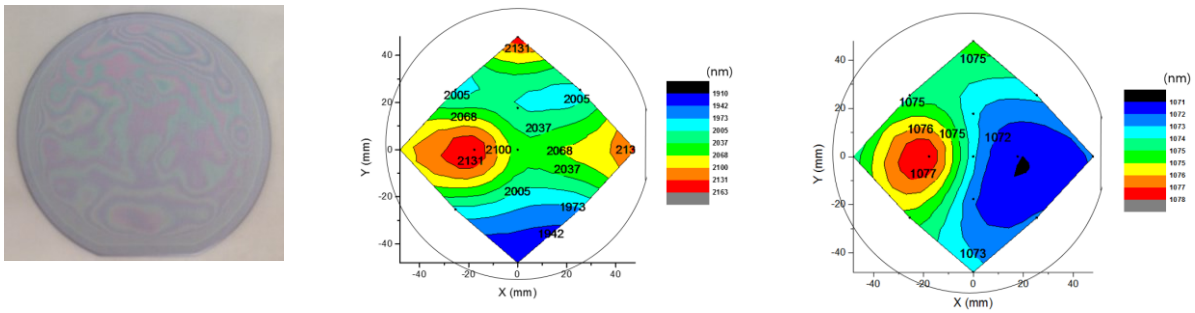

(a) (c) Thickness distribution of Si layer (d) Thickness distribution of BOX layer

Figure 4.1 (a) the used SOI wafer and (b) its box with details from SEH. (c), and (d) shows the uniformity of each layer measured by Filmetrics.

4.1.2. Thin film thickness measurement system: Filmetrics

Thickness measurement uses the phase difference between the each reflected light at each boundary. To improve the accuracy, the wavelength length has a range from 400nm to 1000nm. However, there are still some cases having similar plots. For instance, two different kinds of multi-layers which have almost same phase difference can have the same reflectivity plots. Hence, the knowing the expected thickness of each layer is required before measuring to compare the calculation and measured value.

The thin film thickness measurement system, Filmetrics, consists of broadband light source

and spectroscope as seen in Figure 4.2. Before measuring the thickness of a thin film, calibration is required using the reference wafer. After setting the baseline, the test SiO_2 wafer can be used to check the system. The oxide thickness of the test wafer is 917.4 nm and it will be shown on the monitor if the calibration was fine as shown in Figure 4.2 (c). When the measured data and the calculation data almost overlapped, measuring is fine. Normally, the reliable measurement result shows the fitting error less than 0.1 as shown in Figure 4.3 (fitting error is 0.068792).

(a) (b) (c)

Figure 4.2 The thin film measurement system; Filmetrics (a) the broadband light source, (b) the measuring stage and two reference wafers, (c) the measurement of the test wafer. The red line is the calculation result, and the blue line is the measured data

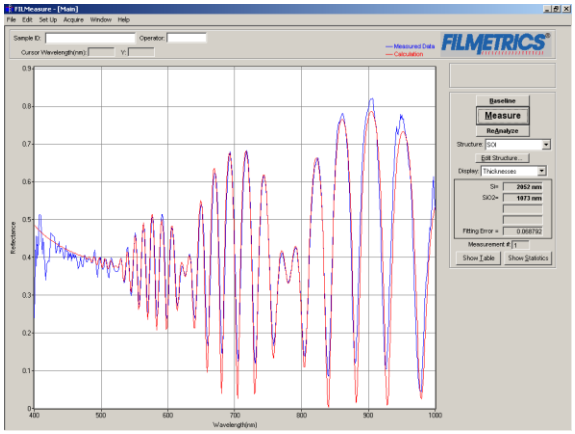

Figure 4.3 Measurement of the SOI wafer

The system measures only one point at a time. To measure the uniformity of a whole wafer, it requires moving the wafer by hand. Furthermore, there are other approximations at the thickness measurement. The first approximation is using the saved refractive index data. In the software, there are about a hundred material data for the layer edit. Each refractive index data represents each specific material which means all silicon dioxides have the same refractive index at a specific wavelength even if they can have a different density as a result of the different fabrication process. For instance, the density of the oxide film by e-beam evaporator is less than the density of dry oxidation. However, there is only one oxide data in the software. This approximation makes a difficulty to find a good fitting when there is some difference between the refractive index data and a real material.

The second approximation is the limitation of measurement. This system cannot measure the thickness less than 10 nm accurately. Therefore, the native oxide layer was normally ignored as an assumption. These approximations make a few nanometer difference at least.

4.2. Waveguide patterning

After checking the uniformity of the SOI wafer, RCA cleaning and lithography were performed with a designed mask and negative photoresist. In this chapter, the designed masks and lithography process are introduced.

4.2.1. Designed Masks

The masks were designed for two types of devices, the plasmon effect MZM and the thermo-optic effect MZM. The plasmon effect device needs P-N junction, and the doping

zone was designed 180-degree symmetry so that the doping zone mask can be used for both P and N doping zones by 180-degree rotation. So, there are three different masks for three different layers as shown in Figure 4.4.

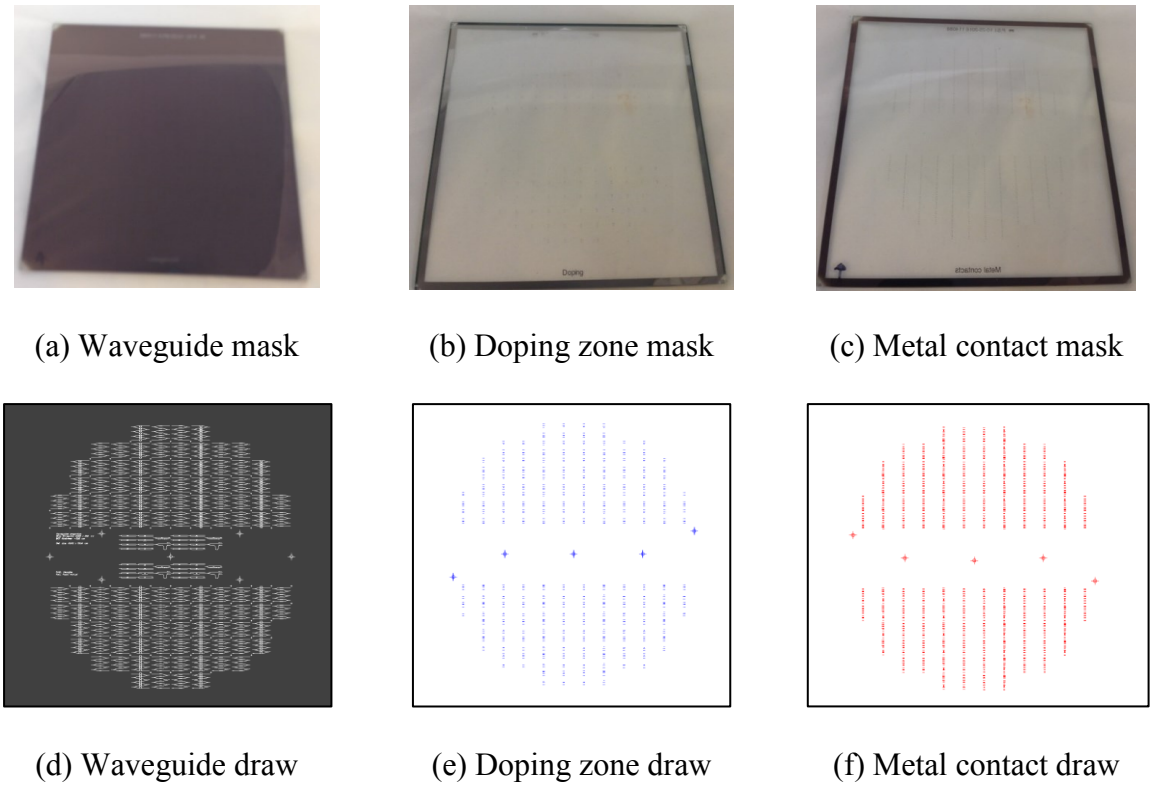

(a) Waveguide mask (b) Doping zone mask (c) Metal contact mask

(d) Waveguide draw (e) Doping zone draw (f) Metal contact draw

Figure 4.4 The designed masks for a 4-inch wafer

However, the device for this thesis needs only the waveguide and the metal contact. Hence, only two of them were used, and the Figure 4.5 shows the overlapping the waveguide and the metal contact drawing only for thermo-optic devices. The mask was designed symmetrically, so all the quadrants are mirror symmetry. In the waveguide mask, there are three different cells, which have a different shape of reference arms as shown in Figure 4.6.

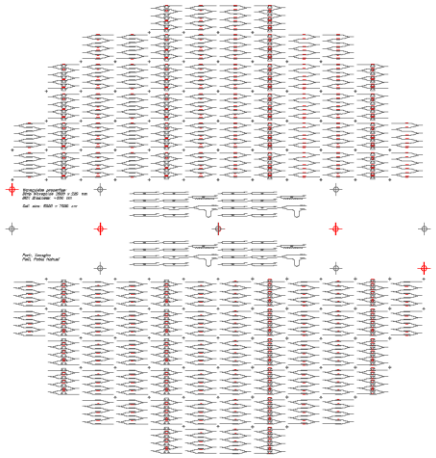

Figure 4.5 Waveguide and metal contact draw

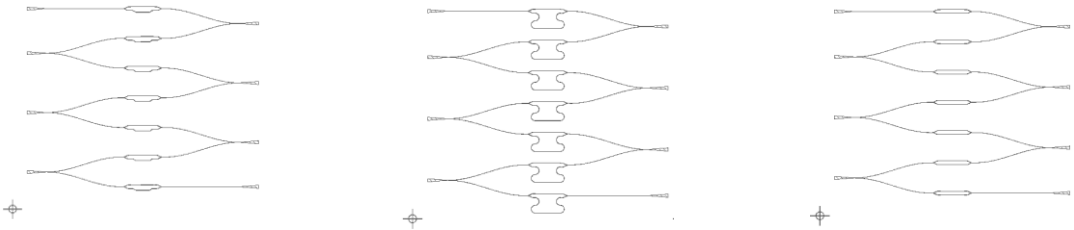

(a) Cell 1 (b) Cell 2 (c) Cell 3

Figure 4.6 The cells in the waveguide mask

In each cell, there are seven Mach-Zehnder Interferometers (MZI) connected to four input/output edge couplers. As seen in Figure 4.6, the MZI in cell 1 and cell 2 were designed to be normally closed by having the different reference arm length, and the MZI in cell 3 was designed to be normally opened by having the same reference arm length. Even though they have different reference arm, the three cells have same devices as shown in Figure 4.7. As mentioned before, the doping process is not required for thermo-optic devices. The image without the doping zone is shown in Figure 4.8. In a cell, only the three

devices having the heat pads can be tested as thermo-optic modulators.

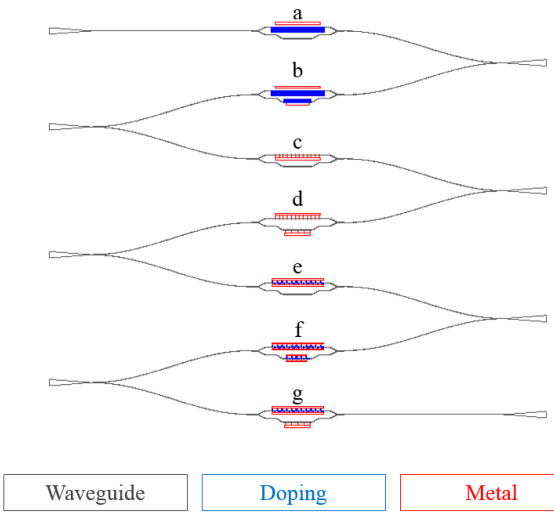

Active Zone		Seven different kinds of modulators
a	P-N junctions	Single drive large P-N slab on one branch
b	P-N junctions	Dual drive balanced P-N slab on two branches
c	Heater	Single Drive Heater
d	Heaters	Dual Drive Heater
e	P-N junctions	Single drive P-N dots array
f	P-N junctions	Dual drive P-N dots array
g	Mixed	One branch with heaters the other with P-N dots array

Figure 4.7 The seven different modulators in a cell

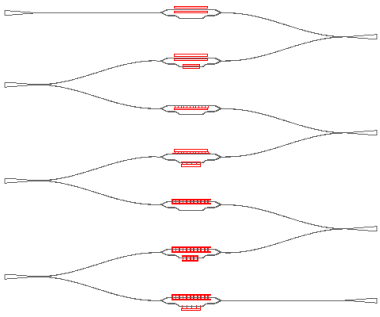

Figure 4.8 The cell 1 of the waveguide mask with metal contacts

4.2.2. Lithography

Before starting the lithography process, the first thing that we have to do is measure the intensity of UV light of the mask aligner as shown in Figure 4.9. From a practical standpoint, it is difficult to perform every single time, but it is recommended for the first time or right after changing a bulb.

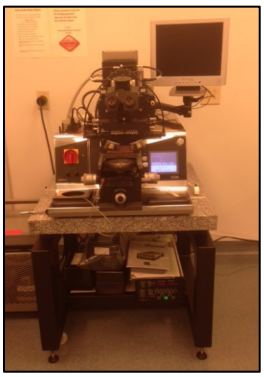

Figure 4.9 The mask aligner MJB4 by SussMicrotec Co.

The second step is cleaning the mask carefully because the mask aligner uses a hard contact method to minimize the diffraction of the UV light. The hard contact makes a better resolution, but the mask is contaminated by the photoresist every time after exposure. Therefore, cleaning the photomask is essential especially for the waveguide mask. At first, just rinsing the photomask with acetone, methanol, and isopropyl alcohol was conducted. However, it didn't clean all the contaminations around the pattern as shown in Figure 4.10 (a). Thus, a certain clean recipe was found [28], and it is shown in Table 4.2. The recipe is one of the simple method but takes more than 30 minutes.

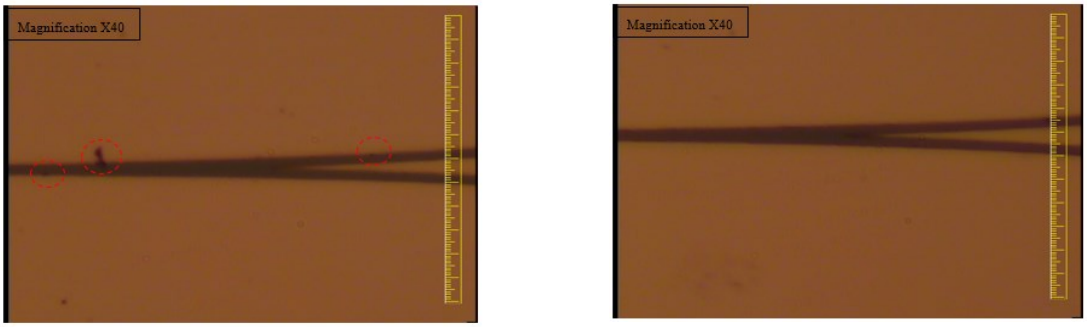

(a) (b)

Figure 4.10 The image of the photomask (a) after acetone/methanol/isopropyl alcohol rinse, and (b) after the photomask cleaning

Table 4.2 The recipe for cleaning the photomask [28]

Preparation	Fill the two Pyrex dishes with acetone and IPA respectively. Pour enough solvent to ensure a total immersion of the mask.
Cleaning	1) Soak the mask in the acetone for 10min. Manually stir every 2 minutes by slightly lifting one side of the dish. 2) Soak the mask in the IPA for 10min. Manually stir every 2 minutes by slightly lifting one side of the dish.
Rinsing	1) Remove the mask from the IPA and soak it in the DIW bath. 2) Start a 3-cycle DIW rinse. 3) Nitrogen dry the mask using the blowgun.

The last step before lithography is cleaning the wafer using RCA clean method. There are two steps in the RCA clean for removing organic dirt and metal ions respectively as represented in tables below.

Table 4.3 RCA1 procedure; 1:1:5 = NH_4OH: H_2O_2: H_2O

1	**Add 30ml NH_4OH (Ammonium Hydroxide) to 150ml deionized water in a petri dish.**
2	Heat to 70-80℃ on hotplate
3	Add 30ml of H_2O_2 (Hydrogen Peroxide)
4	Immerse the wafer for 10 minutes
5	Rinse wafer with deionized water
6	Spin wafer dry

Table 4.4 RCA2 procedure; 1:1:6 = HCl: H_2O_2: H_2O

1	**Add 30ml HCl to 180ml deionized water in a petri dish.**
2	Heat to 70-80℃ on hotplate
3	Add 30ml of H_2O_2
4	Immerse the wafer for 10 minutes
5	Rinse wafer with deionized water
6	Spin wafer dry

For the waveguide patterning, the reversible photoresist AZ 5214 was used as a negative photoresist. To use it as a negative photoresist, it needs two exposure steps which are a first exposure and a flood exposure. The specific information about AZ 5214 is represented in APPENDIX A. The recipe for the fabrication is represented in Table 4.5. In the manual, using HMDS is recommend to improve the adhesion of the photoresist. However, it didn't give a great result during the etching process, because the sticky property of HMDS causes thicker residual after development.

Table 4.5 AZ5214(-) lithography process

#	Process	Details
1	Dehydration after RCA clean	120℃, 3 min
2	Spin resist on a wafer	3250 rpm, 40 sec
3	Prebake	110℃, 1.5 min
4	Exposure	~15mJ/cm^2→ 0.6~1sec

5	Reversal bake	120℃, 2 min (most critical step)
6	Flood exposure	>200mJ/cm^2→ 8~10sec
7	Development	Microposit 351 developer (diluted with DI water in a ratio of 1:3) ~25 sec by hand
8	Post-bake	120℃, 50 sec
9	HF short dip	2~3 sec

Normally, people who are making the micron feature patterns use reactive ion etching (RIE) to etch their silicon layer. However, the only thing I could do is using XeF2 etching system instead of PECVD in the Rose-Hulman clean room because of the unstable condition of the machine and a lack of knowledge. In this limited condition, the residual photoresist should be considered. It is the leftover few nanometers of photo resist on the open area after development that blocks the etching process. To solve the blocking problem, HF short dip is required. The lithography result is seen in Figure 4.11.

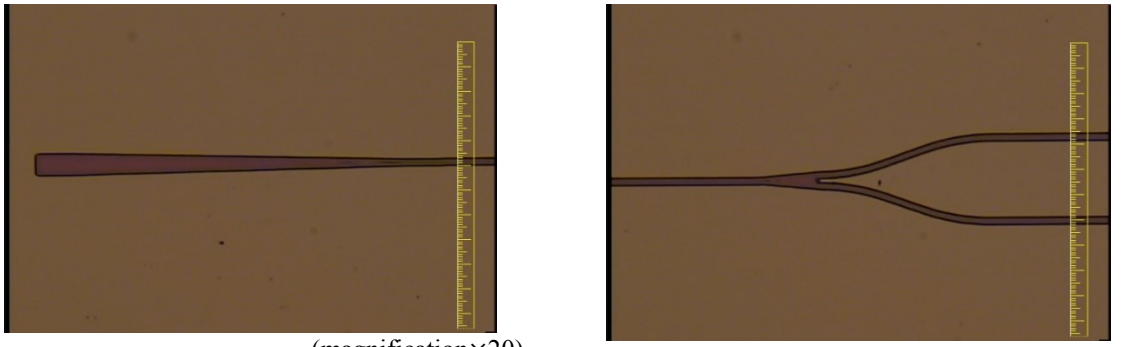

(magnification×20) (magnification×20)

(a) Edge coupler (b) Y-branch

Figure 4.11 The width of waveguide is 3.9±0.2 μm.

4.2.3. Si etching; XeF_2

Normally, etching is performed after lithography. However, there is a very important process between the lithography and the XeF_2 etching. Because the surface condition of the wafer significantly affects the etching results, there should be nothing on the Si layer. The problem came from the photoresist even after development. Normally, there is residual photoresist after lithography process. The organic residual prevents the XeF_2 gas not to be etched which makes an irrevocable failure as shown in Figure 4.12 (a). The XeF_2 etching started from the edge of the wafer, and some part of the wafer surface was not etched properly due to the organics especially around the middle area.

(a) (b)

Figure 4.12 The XeF_2 etching results; (a) without HF dip, and (b) with HF short dip

To solve this problem, HF etching was conducted for 2 seconds as mentioned in the previous chapter. After the HF short etching, the PR organics of atoms thick was removed, and p-Si was etched well as shown in Figure 4.12 (b). The different color rings were exposed after the etching process and the p-Si layer on the very edge was fully etched due to the poor uniformity of p-Si layer.

The XeF_2 etching is one of the general methods to etch the Si layer isotopically, and the machine is shown in Figure 4.13. The etch mechanism is represented in below chemical

formula [29].

$$2\ XeF_2 + Si \rightarrow \quad 2\ Xe\ (g) + SiF_4\ (g)$$

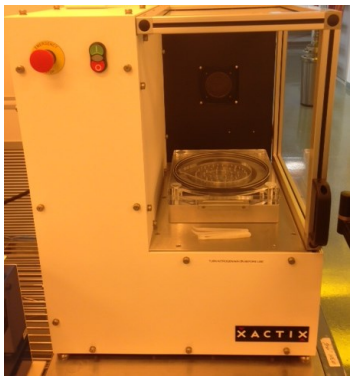

Figure 4.13 The XeF_2 etch machine made by XACTIX (SPTS)

Even if the chemical reaction looks simple, there are several parameters affecting the etch rate or its result. First of all, the parameters that we can control are the pressure of gases, etch cycles, and etch time as seen in the Figure 4.14.

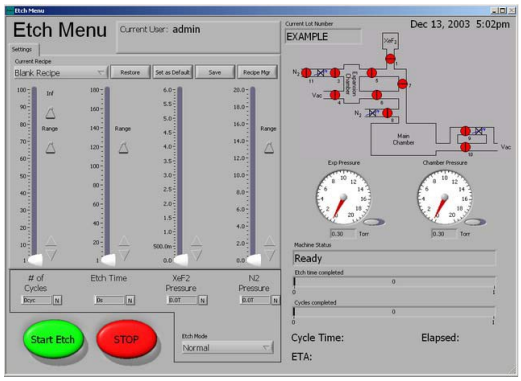

Figure 4.14 The control monitor of XeF_2 etch software

The number of cycles can be changed during the process and the etch time is the time to get the decided XeF_2 pressure. If the etch time is too short compared to the gas pressure, the gas flow could be too fast to etch uniformly. The N_2 pressure effects the straightness of XeF_2

gas. To inject the N_2 gas, the etch mode in the control monitor should be changed to the advance mode. Another parameter that is not included in the control monitor is the area ratio between silicon and etch stop. For these reasons, it is difficult to define the etch rate. So, the etching process was stopped when the box layer appeared on the edge of the wafer. The recipe is represented in Table 4.6.

Table 4.6 The XeF_2 etch recipe

# of Cycles	Etch time	XeF_2 Pressure	N_2 Pressure
12	5 sec	3 Torr	0.8 Torr

4.2.4. O_2 Plasma Asher

The next step before the metal deposition is removing the photoresist on the waveguide because the thickness of the photoresist is about 1.4 μm which is adequate to reduce the heat transfer rate. Besides, the photoresist is not helpful to deposit the metal on the waveguide due to the large difference of Thermal Expansion Coefficient (CTE) of the photoresist and the metal.

There are several methods to remove the photoresist such as using acetone, remover, or plasma asher. The method is decided depending on the photoresist, and the AZ 5214 after hard bake needs the plasma asher to be removed clearly.

Oxygen plasma is monatomic oxygen, created by oxygen gas to an RF electrical field under vacuum. The monatomic oxygen is reactive with organic materials due to the unpaired valence electron. The product of the reaction between the free radical and organics is ash, which is extracted by the vacuum pump. The machine and the recipe are shown in Figure

4.15.

(a)

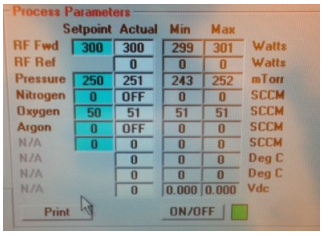

(b)

Figure 4.15 (a) the plasma asher, and (b) the used recipe

Table 4.7 shows the pattern after each process from lithography to removing the photoresist. The removed photoresist by the plasma ash can be checked by the color change of the waveguides. Besides, the width of waveguide at each process is different. Before removing the photoresist, the width of the waveguide is about 4 μm. On the other hand, after removing the photoresist on the waveguide, the width of the waveguide is about 3 μm as a result of the isotropic etching.

Table 4.7 The patterning process

Process	Pattern image (magnification×40)	Width of waveguide
Lithography	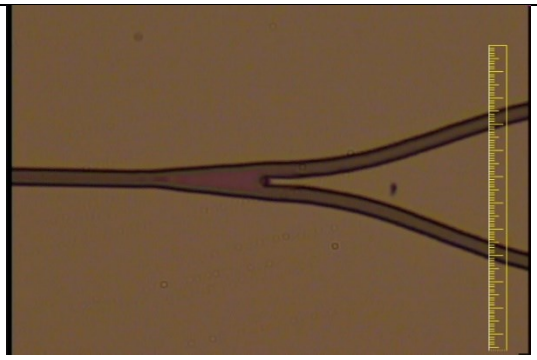	3.9±0.2 μm

XeF_2 etch	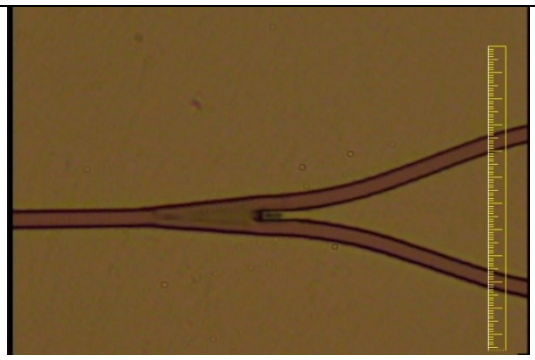	3.9±0.2 μm
Plasma ash	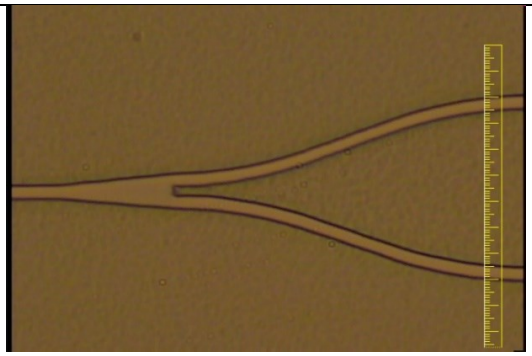	3±0.2 μm

After all the patterning process, one of the waveguides was checked by the scanning electron microscope (SEM, Hitachi High-Tech TM3000). To see the cross-section of the waveguide, the patterned wafer piece was divided by using the fracture property of the silicon wafer. After cracking the wafer piece, the clean image of the cross-section plane was taken as seen in Figure 4.16. The thickness of the etched silicon is about 600 nm and the thickness of the rip waveguide is about 2 μm.

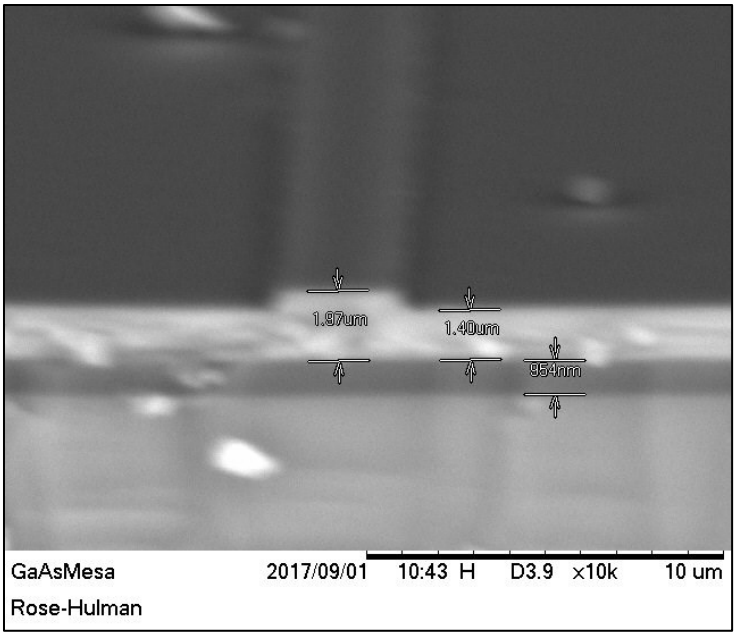

Figure 4.16 Cross-section of the waveguide after patterning process

As seen above, each layer of the SOI wafer is seen clearly, and the represented thickness of each layer is almost the same as the thickness measurement by the Filmetrics.

The unwanted result which is the less-etched Si layer is seen. However, the dimension of the above rib waveguide is working for 1st and 2nd mode light which was checked by Lumerical MODE Solutions as shown in Figure 4.17.

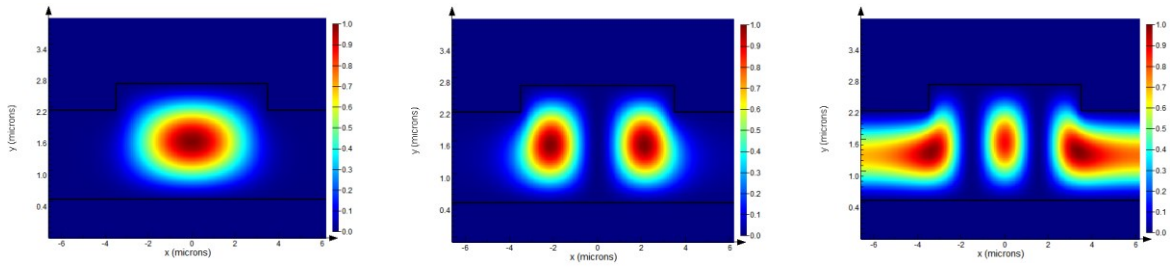

(a) 1st TE mode (b) 2nd TE mode (c) 3rd TE mode

Figure 4.17 The simulation of the fabricated rib waveguide. The confinement of the waveguide is getting reduced from the 3rd TE mode.

4.3. Metal Contact

After the waveguide patterning, the next step is the Ni deposition for the metal contacts. The reason for using Ni is the high resistivity which is for more temperature variation as a heat pad [30]. Before the Ni deposition, the SiO_2 layer of 50 nm thick was deposited to protect the waveguide and to reduce the CTE difference [31] [32]. The dimensions of the metal contacts are L_1=620 µm, t_1=10 µm, L_2=560 µm, and t_2=28 µm as shown in Figure 4.18.

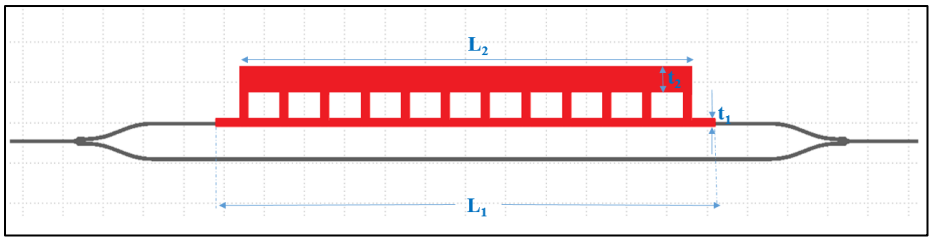

Figure 4.18 The designed metal contact on the waveguide. L1=620 µm, t1=10 µm, L2=560 µm, and t2=28 µm

4.3.1. E-beam evaporation

The e-beam evaporator shown in Figure 4.19 (a) was used for SiO_2 and Ni deposition. The concept of this machine is using e-beam to evaporate the material pellets in the crucial so that the vaporized material can be diffused and deposited on the wafer.

(a) (b)

Figure 4.19 E-beam evaporator and the nickel pellets

The thickness of Ni layer was measured using a profilometer shown in Figure 4.20. The probe of the profilometer contacts the not deposited area then moves to the deposited area to measure the height variation. It is affected a lot by the surface condition, so it needs several measurements to confirm its measurements. As shown in Figure 4.21, the thickness of Ni layer is about 200 nm as the crystal monitor of the e-beam evaporator showed.

(a) (b)

Figure 4.20 (a) The profilometer KLA Tencor D-500, and (b) a wafer after Ni deposition.

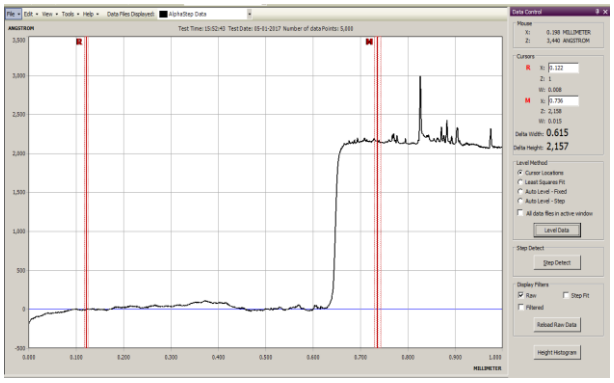

Figure 4.21 The thickness measurement using the profilometer.

4.3.2. Lithography for the metal contacts

After nickel deposition, the next step is the 2nd lithography for the heat pads. For this process, the positive photoresist SRP3622 was used because it is easy to handle and has a recipe in the clean room. The used recipe is represented in Table 4.8. The details about the photoresist are shown in APPENDIX B.

Table 4.8 SRP3622 lithography process

#	Process	Details
1	Prebake	90℃, 1min
2	Spin resist on a wafer	5500 rpm, 60 sec
3	Prebake	90℃, 1 min
4	Exposure	3 sec
5	Post-exposure bake	110℃, 1 min
7	Development	Microposit 351 developer (diluted with DI water in a ratio of 1:3) 30~40 sec by hand
8	Post-bake	110℃, 2 min

Normally, the post-bake is performed for more than 3min to harden resist. However, it was conducted only for 2 min not to damage the Ni layer by the CTE difference.

After the post-bake, it does not need HF short dip unlike the AZ5214 lithography because of its less sticky property and the short bake time.

4.3.3. Ni etching

The etchant recipe for the Ni etching is Di water 50ml, nitric acid 50ml, and acetic acid 10ml [33]. On average, it took 5 minutes at room temperature. During the etching, a proper agitation is required until all of the Ni layer, except for the metal contact, has disappeared. The Figure 4.22 shows the result of the Ni etching process. The waveguide is supposed to

be centered on the heat pads, but there was about a 3 μm misalignment. Even though it was not the perfect alignment, the heat pads cover the waveguide properly as shown Figure 4.22 (b).

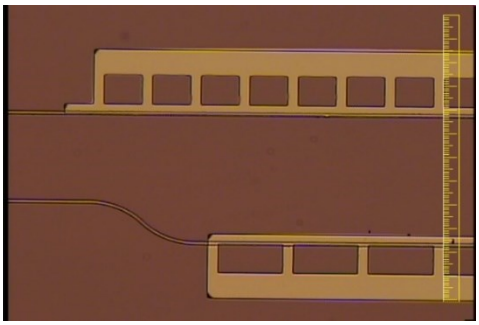

(magnification×20)

(a) by microscope (b) by SEM

Figure 4.22 The metal contacts on the waveguide.

4.4. Wafer cut

The fabricated cells on the wafer were cut by the saw machine shown in Figure 4.23. The saw of the machine is a diamond blade, and its kerf width is from 20 μm to 25 μm according to the manual of the blade. Therefore the width should be considered before cutting the wafer. Unfortunately, the cutting plane is not smooth enough for the edge coupler as seen in Figure 4.24.

(a) (b)

Figure 4.23 (a) the saw machine (Disco DAD-2H/5), and (b) diamond blade

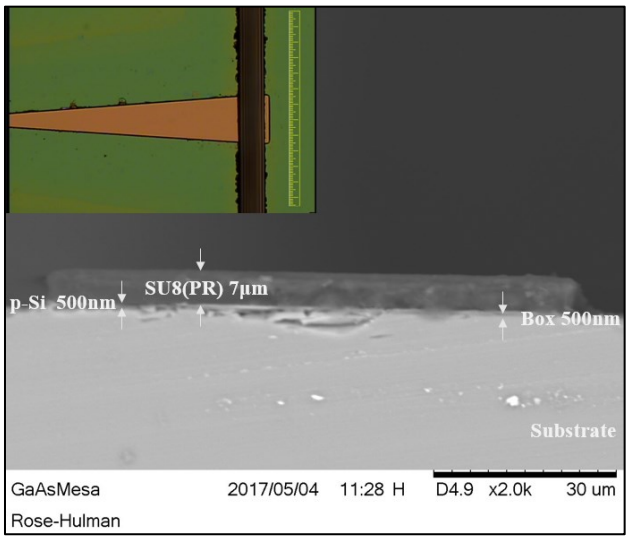

Figure 4.24 An example of a bad cutting. The device was fabricated using SU 8-5 photoresist which is unremovable, and very sticky. Hence, the rough surface of the thick PR is seen very clearly.

For this reason, some space between the edge coupler and the cutting plane is required not to have the rough surface on the edge coupler even if a new blade was used. Figure 4.25 shows that (a) the cutting lines, and (b) its roughness.

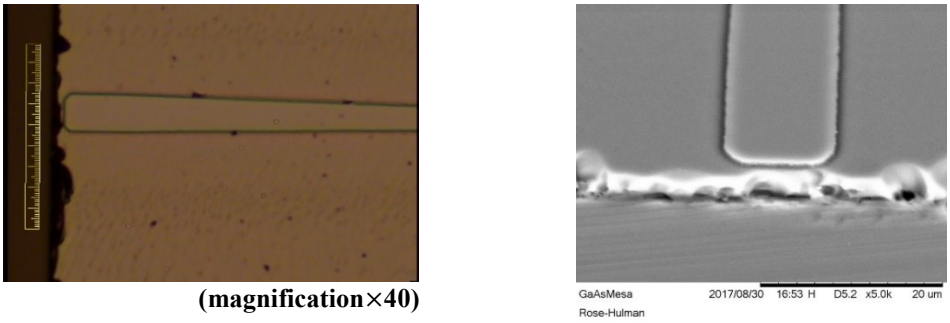

(magnification×40)

(a) **(b)**

Figure 4.25 (a) Top view of the edge coupler by microscope. (b) The cutting plane by SEM is not smooth. On the other hand, the end of the coupler was not damaged during the sawing process due to the few micron space

4.5. 2nd fabrication process: Lift-off

As mentioned in the introduction chapter, at first, the project was making the p-Si waveguide device, but it was stopped due to the loss problem. However, some useful experiments during the fabrication were verified. Here, the simpler and better method, lift-off process, is introduced.

The concept of the lift-off method is making the sacrificial layer before the deposition of the desired material as represented in Table 4.9. The process was to fabricate the p-Si waveguide, but it is recommended to make the heat pads instead of using the normal etching process. Because the lift-off process brings the smoother surface than XeF_2 etching, it is not necessary to worry about the over-etching.

Table 4.9 Lift-off process for the p-Si waveguide

Etch-less Fabrication Process		
1	Wet Oxidation; Furnace	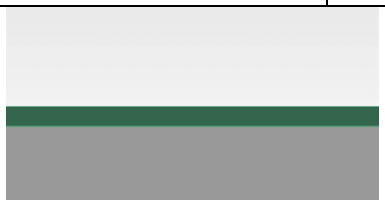
2	Lithography; SPR 3622	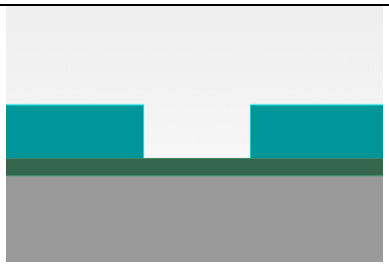

3	a-Si deposition; Sputtering	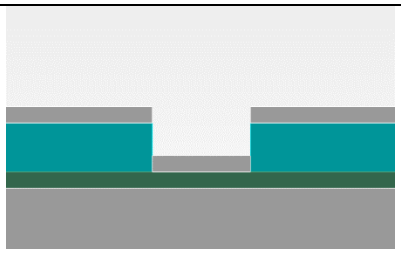
4	Lift-off; acetone & Annealing; Furnace	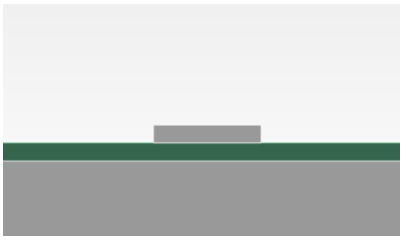

After the oxidation of the box layer, a positive photoresist SPR 3622 was used as a sacrificial layer. It is relatively developed better than the photoresist AZ5214which needs the HF short time dip for the next process. The wafer after lithography can be deposited by the sputtering machine without any problem as seen the Figure 4.26 (a).

The next step is the lift-off to remove the sacrificial layer and the a-Si on it. The boiling acetone was used to make it faster as shown in the Figure 4.26 (b). The temperature of acetone was between 50~60℃ for 5mins. Most of a-Si on the photoresist was removed easily, but some area which has no pattern requires the more physical stimulation such as an agitation or the ultra-sonic.

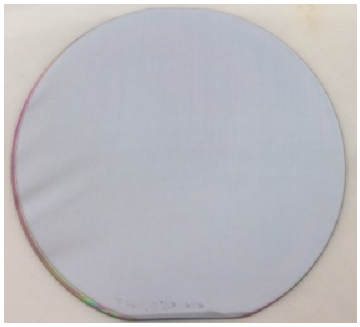

(a) after a-Si deposition

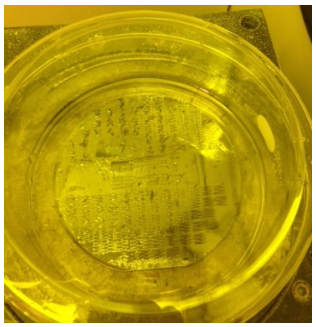

(b) Lift-off using the boiling acetone

Figure 4.26 (a) The patterned wafer after the silicon deposition, (b) in the boiling acetone to remove the sacrificial layer and a-Si via lift-off

Figure 4.27 is to compare the two waveguides by the two different fabrication processes. The waveguide formed by the etching process has the thinner width because of the isotropic etching. The surface roughness of the etched waveguide is worse than the one fabricated by the lift-off process. Because the uneven surface was magnified during the XeF_2 etching. Besides, the p-Si waveguide in the edge of the wafer is etched more than the waveguide in the middle due to the bad uniformity of the silicon deposition. All the problems lead to the lift-off process to fabricate the better silicon waveguide. Therefore, the lift-off process is better than using XeF_2 etching or other wet etching in case there is no RIE system. For the metal contacts, this etch-less process was confirmed and is recommended.

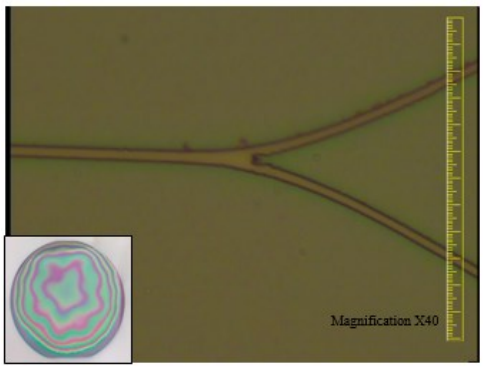

(a) Waveguide width = 3±0.2 μm

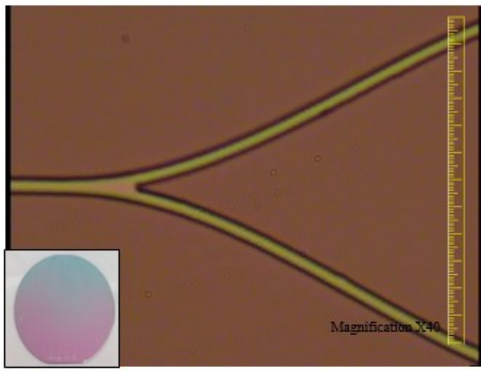

(b) Waveguide width = 3.9±0.2 μm

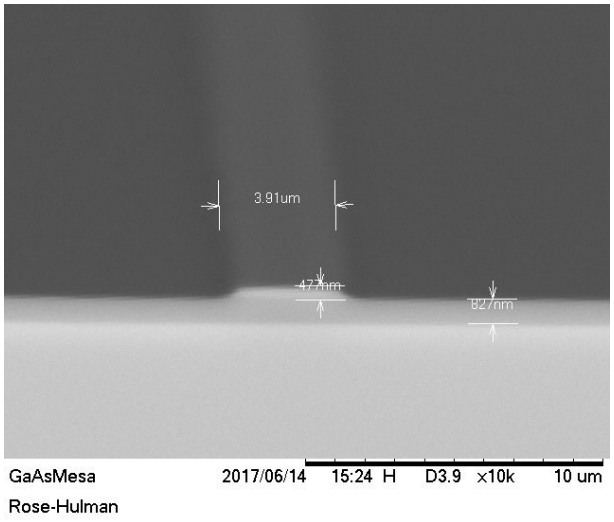

(c)

Figure 4.27 The p-Si waveguide by (a) the XeF_2 etching, and (b), (c) the lift-off process. (c) The SEM image shows the cross-section of the waveguide formed by the lift-off.

4.6. Failures in experiments

In this chapter, some experiments are introduced to avoid the same mistakes. These attempts were to get the polycrystalline silicon waveguides but failed for some reasons.

4.6.1. Polycrystalline silicon

The process began by preparing SOI wafers using a furnace and a sputtering machine. Making SOI wafers doesn't have a great efficiency due to the characteristic of polycrystalline silicon. The silicon can be classified depending on its crystal structure as a single crystal, polycrystalline, and amorphous silicon. Naturally, the three kinds of silicon have slightly different refractive indexes due to the different density range from 2.285 g/cm^3 (a-Si) to 2.329 g/cm^3(single crystal) [34]. Most importantly, the refractive index of polycrystalline silicon (poly-Si) and amorphous silicon (a-Si) depends on its fabrication recipes [35]. Hence, measuring the thickness of non-single crystal silicon film using the filmetrics or the ellipsometry has an unavoidable uncertainty. Furthermore, the anisotropic etching cannot be adjusted to the p-Si due to the all direction crystal planes. Despite these difficulties, p-Si was chosen as a core material so that the study of Si photonic device begins without the burdensome SOI wafer cost.

Table 4.10 The amorphous silicon on the oxide layer

Process		Si SiO_2 Ni AZ 5214 SPR 3622
1	Wet Oxidation; Furnace	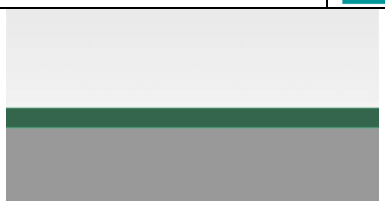

2	Si Deposition; Sputtering machine	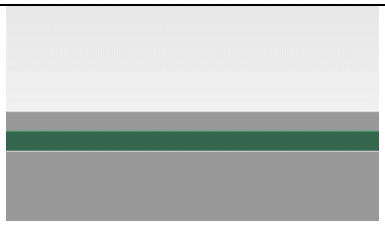
3	Annealing; Furnace	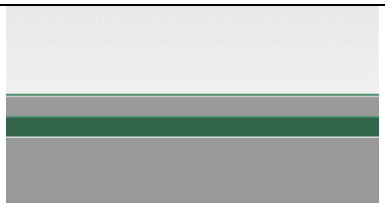
4	Oxide Etching; BOE	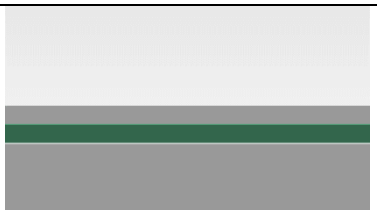

4.6.1.1. Wet Oxidation

The first layer to be fabricated the waveguide is a silicon dioxide layer called BOX on a bare silicon wafer. The used wafer is a (100) 4-inch wafer. Before the BOX layer process, cleaning the wafer surface is essential to remove organic, ionic, and metallic contaminations.

There are two kinds of oxidation; dry and wet oxidation. The environment of the dry oxidation is a pure oxygen gas (O_2) with the high temperature to obtain the oxide layer faster as seen in Figure 4.28 (a). The chemical reaction of dry oxidation is only between silicon and oxygen gas as represented in equation (27). On the other hand, the atmosphere of wet oxidation is water vapor (H_2O) and a pure oxygen gas (O_2) as represented in equation (27) and (28). The hydroxide (OH^-) diffuses through the already-grown oxide much quicker than oxygen gas (O_2). Hence, the wet oxidation has much higher oxidation rates than dry

oxidation as shown in Figure 4.28. However, the oxide layer from the fast oxidation has more pores which is a worse diffusion barrier.

$$\mathrm{Si} + O_2 \rightarrow SiO_2 \tag{27}$$

$$\mathrm{Si} + 2H_2O \rightarrow SiO_2 + 2H_{2\,(g)} \tag{28}$$

The oxide layer in this device doesn't need to be a diffusion barrier, since the purpose of the BOX layer is to separate the two Si layers and gain high refractive index difference. Therefore, the wet oxidation process was performed for the BOX layer.

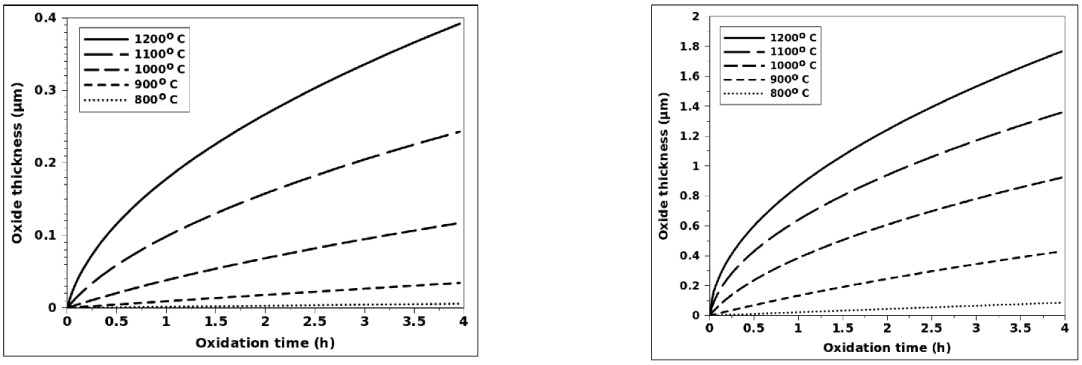

(a) Dry Oxidation (b) Wet Oxidation

Figure 4.28 Oxide thickness versus oxidation time for (a) dry, and (b) wet oxidation of a (100) silicon wafer under various temperatures [36].

The oxide thickness of commercial SOI wafers is 2 μm which is enough as a BOX layer. However, the oxidation time should be longer than 14.5 hours in case of the condition of 1000℃, O_2 10sccm, $H_2O_{(g)}$, and (111) Si wafer. Because of the long process, the thickness of the BOX layer will be between from 500nm to 1,000nm for convenience. To obtain the thickness more than 500 nm, the oxidation time would be more than 2 hours which depends on the process condition. There are lots of parameters affecting the oxidation process, such

as temperature, pressure, gas flow, and the crystal direction of silicon [36].

(a) (b) (c)

Figure 4.29 Furnace for oxidation and annealing. (a) showing the gas flow controller, and the water beaker on the hot plate. (b) showing the side view of the furnace, and the temperature controller. The glove, the wafer boat, and the entrance are shown in the (c).

The furnace shown in Figure 4.29 cannot control all the parameters. For the machine's stability, the temperature in the furnace can be up to 1000℃, and it has no pressure control. Additionally, the oxygen gas and the water vapor came from only the one side of the tube which makes different oxide thicknesses even in a wafer boat.

The used recipe for wet oxidation is 1000℃, O_2 10sccm, and water vapor for more than 2 hours to get thicker than 500nm oxide. The uniformity of oxide layer is good enough for this device as seen in Figure 4.30. The thickness was measured by the Filmetrics.

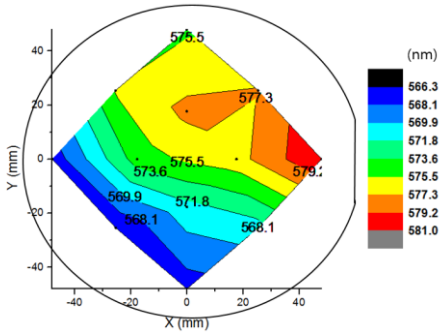

(111) Si wafer

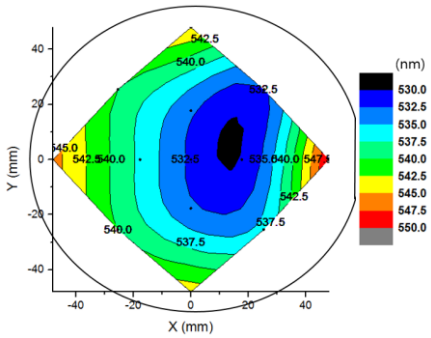

(110) Si wafer

Figure 4.30 Oxide thickness of (111), and (110) wafer after wet oxidation; 2hr, 1000C, O_2 10sccm. The oxide uniformity of the (111) wafer is 1.3% and the oxide uniformity of the (110) wafer is 2.7%. The defined uniformity is U(%)=(max-min)*100/max.

The thickness difference between the maximum and minimum thickness in a wafer is about 10 nm, which is quite good quality for a micro-device. The oxidation results of both wafers in Figure 4.30 were by the same oxidation recipe, but two wafers have a relatively different thickness, distribution, and uniformity. The reasons are due to the different kinds of wafers, the position in the wafer boat, and air flow when they came out from the furnace. Therefore, the rate should be slowed as much as 1 inch per 5 seconds while putting the wafer boat in and out of the furnace.

After oxidation, the wafers show specific color depending on their thickness as seen in Figure 4.31. Therefore, the color of BOX layer was green or purple which would be seen again after waveguide etching process.

(a) 540 nm thick oxide

(b) 680 nm thick oxide

Figure 4.31 (a), (b) shows the different color as result of each thickness [37]. The color chart of the SiO_2 film depending on its thickness is in APPENDIX C

4.6.1.2. Sputtering deposition

The next process to prepare a SOI wafer is silicon deposition. There are several methods to form the silicon layer. One of the methods is using Plasma Enhanced Chemical Vapor Deposition (PECVD). It can form the poly-Si layer without the annealing process if the machine can achieve the temperature more than 600℃. However, the PECVD machine in Rose-Hulman has a temperature limitation of 250℃ for the machine's stability. It requires more time for its process such as load/unload, purge, and pump down. For these reasons, the PECVD is not preferred for Si deposition, and the sputtering machine was used. The magnetron sputtering is a typical process of physical vapor deposition (PVD). The sputtering machine uses plasma by applying a high voltage, which means the silicon structure by sputtering deposition is amorphous. Hence, it requires an annealing process to get the dense structure, polycrystalline silicon, after sputtering deposition. The mechanism of the magnetron sputtering deposition is described in Figure 4.32. To form the plasma, a vacuum with some inert gas (Normally Ar) is required. Then, a high voltage is required to

ionize the inert gas and pull the ions strongly. The high energy ions strike the silicon target on the cathode. As a result, the silicon atoms are ejected by the collision, and then the atoms deposit on all surface in opposite side as result of the principle of action and reaction.

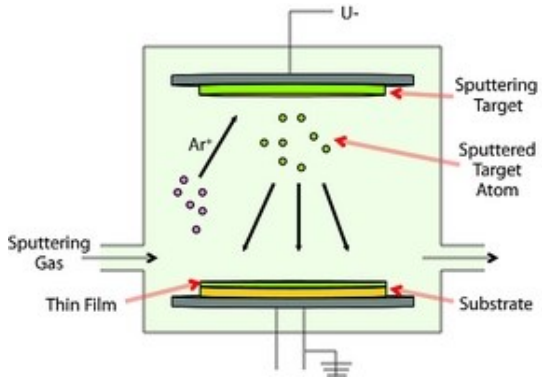

Figure 4.32 Schematic of sputtering deposition process

Figure 4.33 shows the sputtering machine that was made by Kurt J. Lesker Corp and used for this experiment. The gas flow and the voltage are the parameters that can be controlled to get better uniformity of the silicon film [38]. The RF power is used for the insulator materials, and also can be used for the silicon. However, it doesn't form the better uniformity compared to the film formed by DC power. Hence, only DC power was used for convenience.

There are other parameters which effect the uniformity of deposition. One of them is the residual thickness of a target. In case of a new target or a target phasing to life, it showed very unstable deposition rate.

The condition of the sputtering machine was changed several times due to the replacement of the target, and its position for another target during the experiment. For this reason, the uniformity was not same even though an identical recipe was used.

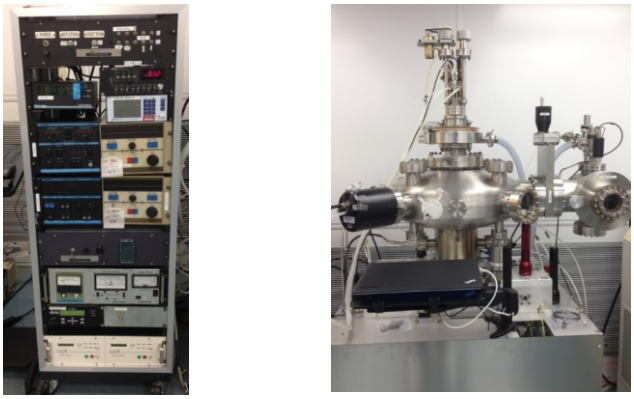

(a) (b)

Figure 4.33 The sputtering machine; (a) controller and (b) a main chamber

Table 4.11 shows a part of the sputtering deposition record. In the thickness section, T is a thickness range, D is the difference between the maximum and the minimum thickness, and U is the uniformity defined below

$$\mathrm{U} = \frac{Max-Min}{Max} \times 100(\%). \qquad (29)$$

According to the sputtering deposition test, the recipe of Ar 50 sccm with DC power 250W made a relatively good uniformity and is a fast process. The uniformity of the sputtering machine, even with the best recipe, is quite bad for MEMS process.

Table 4.11 Sputtering deposition record

Date	Recipe		Time	Thickness		
	Ar (sccm)	DC power (W)		T (nm)	D (nm)	U (%)
Dec. 02. 2016	75	250		372-445	73	16
	75	150		198-231	33	15
Dec. 08. 2016	50	250		240-270	30	12
Dec. 13. 2016	20	250		267-297	30	16.3
	15	250		339-392	53	13.5
	15	200		385-434	49	11.3
	50	100		246-271	25	11
Jan. 05. 2017	25	250		1044-1146	102	8.9
Jan. 06.	25	250		740-856	116	7.4
Jan. 10.	25	250	30min	402-474	72	15.1
Jan. 12.	20	200	40min	538-620	82	11.5
Jan. 17.	50	250	27min	605-668	63	9.4
	50	150	32min	325-374	49	13.1
	50	200	32min	434-498	64	12.8
Jan. 23.	75	250	24min	354-404	50	12.3
	50	250	23min	391-445	54	12.1
	75	290	22min	394-458	64	13.9
	75	150	40min	356-414	58	14

4.6.1.3. Annealing

All properties of materials, including the optical property, are decided by their crystal structure. The structure of the non-single crystal silicon (a-Si, and p-Si) is determined by the fabrication process. Normally, a-Si is formed at below 600℃ and has a small grain size. The amorphous silicon consists of small grains (~50 nm) with lots of defects, which is the main reason for the huge loss. The dangling bonds in grain boundary cause the light absorption. Despite the loss, there is a study which uses the amorphous silicon as a core material through the hydrogen passivation. After the hydrogenation and a proper heat treatment, a-Si can be used as a core material with 3dB/cm loss [39]. Nevertheless, it is still not suitable as an active device due to less electro-optic effect [14]. Although the device in this thesis is not using electro-optic effect, the future work will be the fabrication of MZM device using the Plasmon effect. Hence, the a-Si formed by the sputtering deposition was transformed through the annealing process.

Poly-Si can be deposited by PECVD without annealing process. However, the poly-Si by PECVD consists of the smaller grains than the poly-Si after the annealing process due to the temperature limitation of PECVD machine [40]. Hence, a proper annealing process is required to obtain the lossless poly-Si waveguides. The condition of the high temperature (1100℃) with a pure nitrogen atmosphere provides the lower losses than the condition of a lower temperature (600℃), due to an improved degree of crystallinity [15], [16], [40]. As mentioned in the introduction chapter, the defects in the crystal cause the scattering loss, and the smaller grain size indicates more grain boundaries. The grain boundary is the continuity of the dangling bonds which are the reactive electrons. Therefore, the grain

boundary is the center of the absorption loss. To minimize these losses, high temperature is the key. Thus, the annealing recipe was set to 1000℃ with a nitrogen atmosphere for 60 minutes.

Figure 4.34 shows the p-Si layer before and after the annealing process. Before the annealing process, the surface of the a-Si layer represents only the silver color even if it has a poor uniformity. On the other hand, the p-Si layer has color rings on the surface as a thickness distribution. For comparison, the average thickness is reduced from 514 nm to 449 nm, and the uniformity is improved from 12 % to 11.6 %. The uniformity variation is not only from the crystallization but also the oxidation during the annealing process in the impure nitrogen atmosphere. The furnace has no vacuum chamber, and it is connected to a nitrogen gas generator. So, the atmosphere in the annealing furnace consists of mostly nitrogen and in which a dry oxidation can occur. During the annealing process, the oxide layer of a few nanometers thick is formed and should be removed before the lithography process. For this reason, HF etching was performed, then the thickness of p-Si was measured.

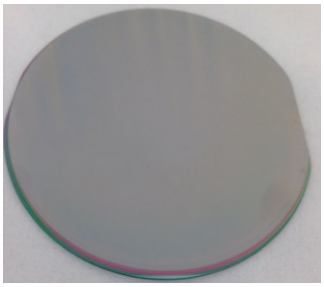

(a) a-Si

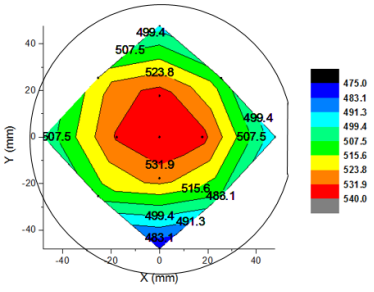

(b) a-Si

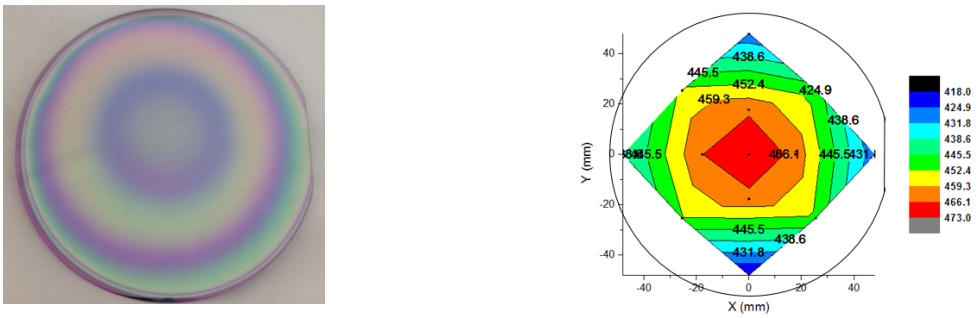

(c) p-Si (d) p-Si

Figure 4.34 (a) a-Si layer after the sputtering deposition, (b) the thickness distribution of a-Si layer, (c) p-Si layer after the annealing process, and (d) the thickness distribution of p-Si layer

To get better p-Si layer as a waveguide material, there are few things that should be improved. The first is the uniformity of the amorphous silicon layer by sputtering deposition. Unfortunately, there is no way to improve the uniformity with the sputtering machine. The second is the annealing temperature and time. As mentioned, the higher temperature makes the greater grain size, but the temperature of the furnace cannot be higher than 1000℃. On the other hand, the time of the oxidation can be longer and should be as long as possible to grow the grain size. Lastly, the hydrogenation was not performed, which is very important to remove the reactive electrons. To perform the hydrogenation, the PECVD machine can be used, but it was not able to do the hydrogenation due to the lack of knowledge and its unstable condition.

4.6.2. KOH etching

The KOH etchant is typically used to etch the silicon and has an advantage due to the

different etch-rate depending on the crystal plane [41], [42]. This property is preferred to etch the single crystal silicon, but it is not for the polycrystalline silicon, which consists of all directional grains. So, the etch rate shows around the average of the etch rate of all crystal planes.

To test the KOH etching, a poly-SOI wafer was prepared as shown Figure 4.35

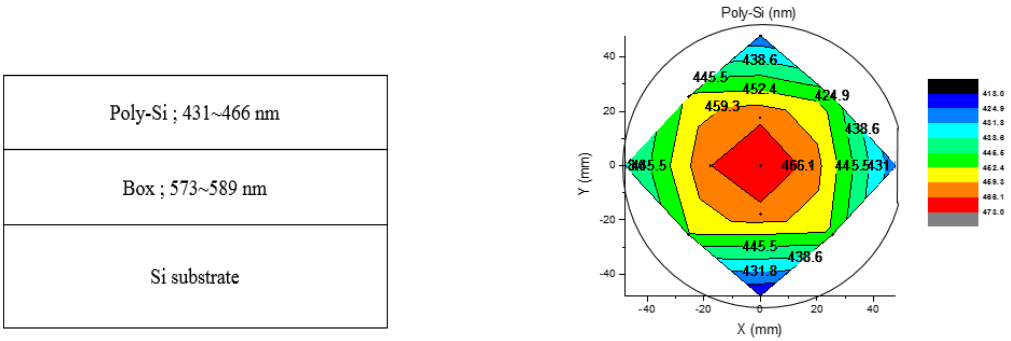

(a) (b)

Figure 4.35 The poly-SOI wafer. The annealing was performed at 1000℃ for 30min.

The KOH etchant was composed of 50g of KOH pellets, 190ml of DI water, and 40ml of isopropyl alcohol. The temperature was kept at 40℃ during the etching test with proper agitation. There were four, 30-second tests. After each etching test, the thickness of the p-Si layer was measured by the Filmetrics. Figure 4.36 shows the result, and the average etch rate is 1.1nm/sec.

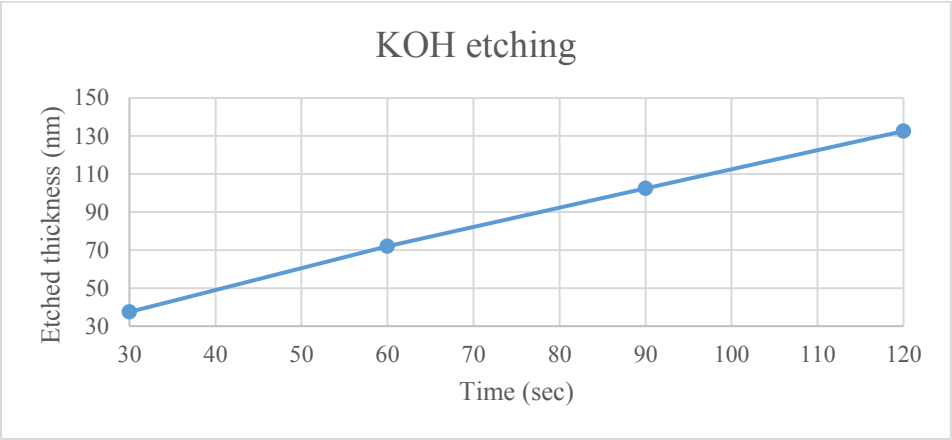

Figure 4.36 KOH etching time versus the etched thickness of p-Si

During the etching test, the entire surface of the wafer etched uniformly. However, it showed a bad result when etching a patterned wafer as seen in the Figure 4.37. For the patterning, the photoresist AZ5214 was used. It requires the HF short dip, which was not performed. The unremoved organics disturbed the KOH etching process and made the film dirty on the surface.

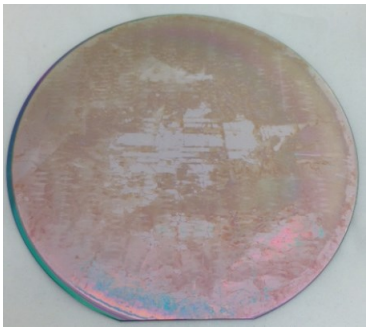

Figure 4.37 A patterned wafer without HF short dip etched by KOH etchant.

Therefore, the HF short dip is an important process after AZ5214 lithography.

5. Experimental Measurement

One of the largest challenges in this work is the optical measurement of the devices. Unfortunately, the optical output could not be detected due to the huge losses. Therefore, in this chapter, the measurement from the setup to the practical problems process is discussed

5.1. Setup

The setup for the measurement is seen in Figure 5.1. Two optical fibers, two electric probe tips, and a vacuum chuck can move XYZ directions respectively.

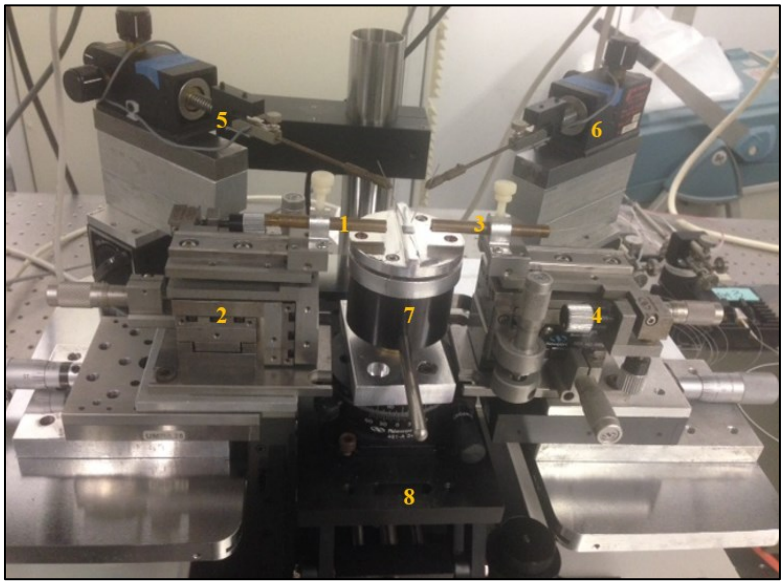

Figure 5.1 Setup for optical measurement; 1.Input single mode fiber and holder, 2.XYZ translation stage, 3.Ouput SMF and holder, 4.XYZ translation stage, 5,6.Electric probe tips and stage, 7.Vacuum chuck, and 8.Stages

The holders for the optical fiber rods and the plate for the small cell were designed and fabricated for this setup because the two fibers with the holders should be closed to the device. The exposed fiber tips from the holders should be very short to reduce the vibration. Around the setup, there are two cameras and some lamps to secure the side view and the top

view as seen in Figure 5.2. The two cameras are connected to a computer through the USB port and a converter to monitor the live image. The camera for the top view is not placed vertically because it is difficult to see the tiny waveguide with the camera when it is placed at the directly above the cell. Hence, the camera was placed with some angle and the side lamp to see the waveguide more clearly.

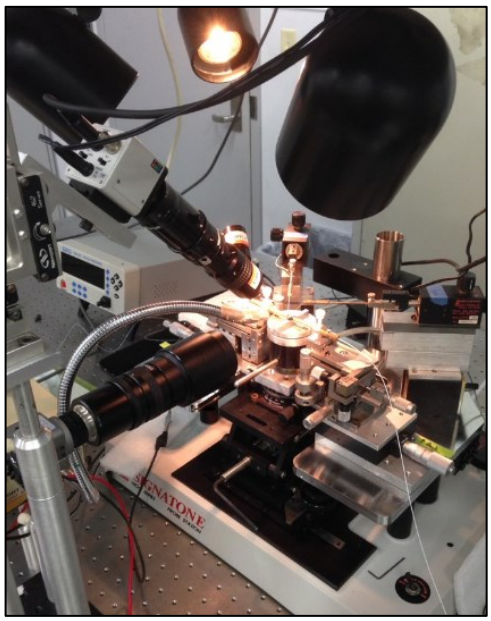

(a)

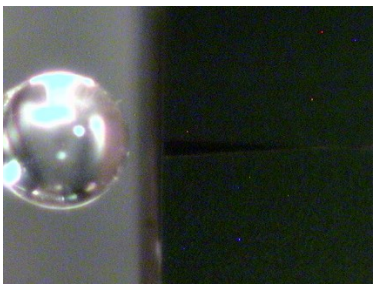

(b)

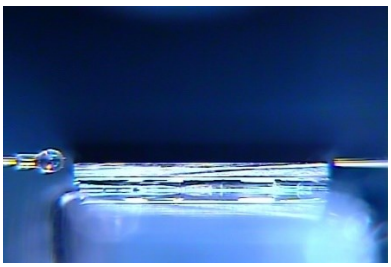

(c)

Figure 5.2 (a) The setup for viewing cameras and lighting lamps, (b) an example of the top view, and (c) an example of the top view

This position is better to secure the device image, but it is not helpful to move any parts along the y-axis through the top view monitor. Despite the angle problem in the top view monitor, it is enough to find a proper position with the adjustment of millimeter unit. To get the more precise adjustment of micron unit, the optical multimeter is required after a proper

position is found through the monitor. The optical and electrical instruments used in the setup are shown in Figure 5.3.

(a) Laser diode controller
(ILX Lightwave LDC-3900)

(b) Laser diode
(Alcatel A 1905 LMI)

(c) Optical amplifier
(IPG Photonics EAD-500-CL)

(d) Optical multimeter
(ILX Lightwave omm-6810B)

(e) Optical spectrum analyzer
(Anritsu MS9710B)

(f) DC power supply
(Agilent E3611A)

(g) Waveform generator
(Agilent 33120A)

(h) Signal oscilloscope
(Agilent 54622D)

Figure 5.3 Optical and electrical equipment for the device test

5.2. Optical fibers and measurement

The next thing to be prepared for the test is the optical fiber to put the light into the device

and to take the optical output. The used fibers are three different fibers as shown in Figure 5.4. This figure also shows the fiber-to-fiber test which was performed after each fiber test. All the fibers used in this experiment are single mode fibers which have a diameter of 8~10 μm in order to reduce the size gap between the fiber core and the edge coupler of 12 μm wide. The cleaved fibers shown in Figure 5.4 (a) were prepared by using the high precision optical fiber cleaver, Fujikura ct-07. The second fiber is a lensed fiber made by Corning OptiFous, and the dimensions are T=826±18 μm, Rc=227±2 μm, f=2.5±0.3 mm, and Mode-Field Diameter (MFD)=62±2 μm shown in Figure 5.5. The last fiber is a tapered fiber made by OZ Optics, and its dimension are SL=7 μm, WD=12 μm, and SD=2 μm shown in Figure 5.6.

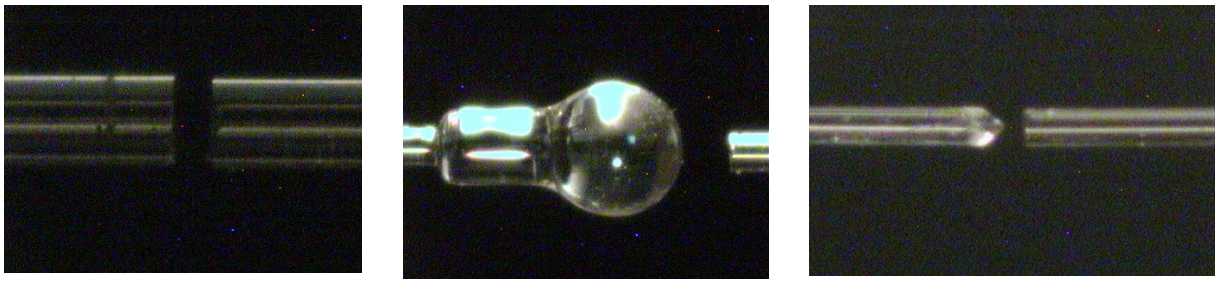

(a) (b) (c)

Figure 5.4 Optical fiber test before the measurement

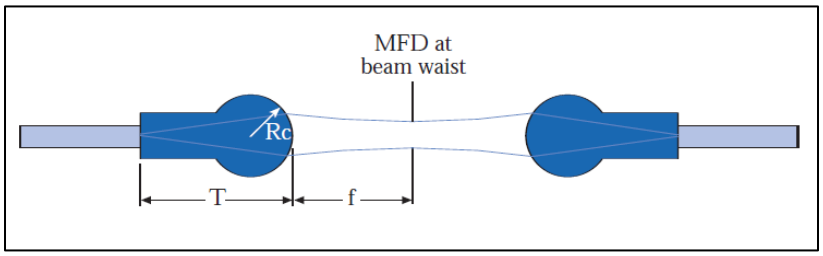

Figure 5.5 Schematic of the lensed fiber[43]

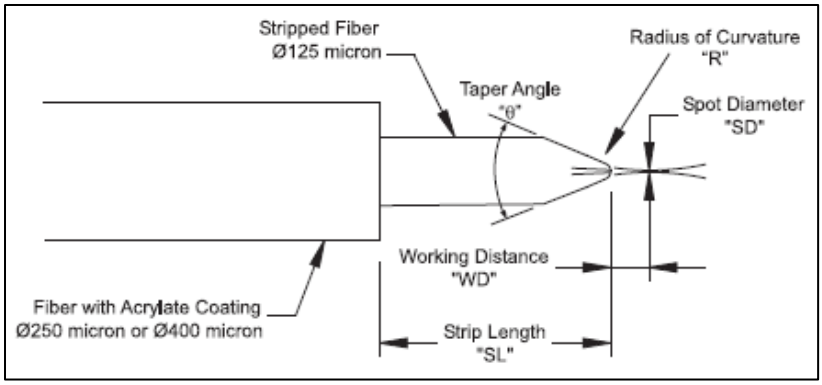

Figure 5.6 Schematic of the tapered fiber[44]

Before doing the fiber-to-fiber test shown in Figure 5.4, there was a fiber test using the optical multimeter to check the loss of each fiber. As a result, the cleaved fiber has 0.4dBm loss, the lensed fiber has a 1.1dBm loss, and the tapered fiber has 1.3 dBm loss. The fiber loss is from the connectors and made by the fusion of the special fiber and a normal fiber. As shown above, each fiber provides different light propagation.

The tapered was chosen as an input fiber and the cleaved fiber was placed in the output position. The reason for choosing the tapered fiber as an input is that the cleaved fiber and the lensed fiber cannot focus on the edge coupler as much as the tapered fiber does due to the bigger diameter than the cross-section area of the edge coupler which means the two fibers must have more insertion loss than the tapered fiber. This is due to the fact that, the light that is not focused on the edge coupler can go through the silicon substrate or pass through above the waveguide. This unwanted light can also be detected by the output fiber which makes the confusion to determine the real optical output.

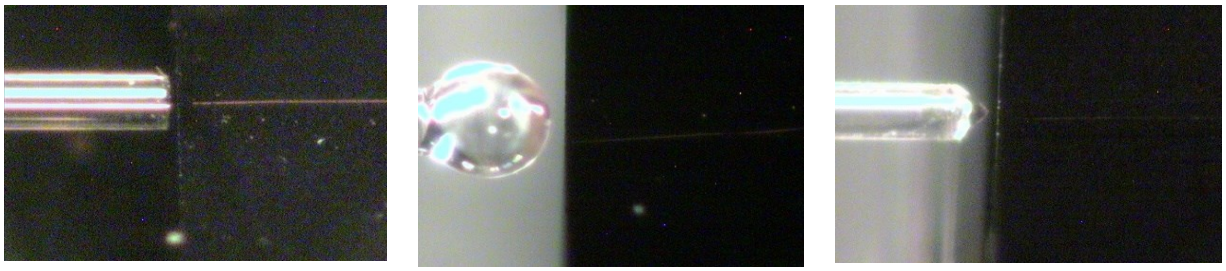

(a) cleaved fiber (b) lensed fiber (c) tapered fiber

Figure 5.7 Measurement with each optical fiber

Even though there were a lot of tries using the best combination of the fibers as well as other combinations as shown in Figure 5.7, it was not able to detect the clear optical output.

Here are the reasons for the optical losses:

1. The loss from the side of the waveguide and the facet of the edge coupler

The waveguide pattern was formed by the XeF2 etching, and the etched surface is seen in Figure 4.16, and Figure 4.25 (b). Unfortunately, the SEM used for this work is not enough to get the clear ×10,000 magnification images, but the rough surface of them is seen. The rough surface makes the scattered light and the scattered light can be higher order mode or escaped. The higher order modes can be confined in the multimode waveguide with low loss, but the fabricated waveguide is a less-etched rip waveguide which can have only five modes including TE and TM modes according to the Lumerical simulation. Hence, it does have a huge loss by the rough surface even though it is a 3 μm wide waveguide. The loss in 2 μm wide, 250nm high, rip waveguides is 0.27 dB/cm [45].

2. The length of the waveguide

The shorter length of the waveguide is better due to the sidewall loss. The length of the device including the two edge couplers and the waveguide is about 4 mm. The length of 4 mm was designed to saw the wafer in the last fabrication step. Because of the wafer thickness of 525 μm, it is difficult to cleave the wafer to be shorter than 2 mm. To do this, the wafer needs to be polished to be shorter. The typical sidewall scattering loss is 2-3 dB/cm for the single mode (500×220 nm) silicon waveguides [46].

3. The lack of the Chemical Mechanical Polishing (CMP) techniques

The CMP process is one of the important process to get the smoother surface after etching or sawing. Especially for the cleaved surface by the sawing machine, it is crucial to get a smooth side of the cell, and to reduce the gap between the side and the facet of the edge coupler. By doing the CMP, the scattering loss and the diffraction loss from the edge coupler can be reduced.

4. Using a half of the SOI wafer

To prepare unexpected problems during the fabrication, the SOI wafer was cut in half and these halves were used separately. Half of the wafer was attached to a dummy wafer using a tape for the PR spin coating process. After the spin coating, the tape was removed, but some sticky glue of the tape still remained. Unfortunately, it was not seen clearly, but the thickness of the glue is thicker than the coated photoresist. This impurity caused the uneven hard contact, so some area of the wafer did not have the hard contact. As a result, some area that had a gap during the exposure step has an expanded or distorted pattern because of the

diffraction effect.

Additionally, the difficulties in the experiment are discussed:

1. The error of the dicing machine

As mentioned in the chapter on the wafer cut, the cutting plane is very rough. Hence, it needs gaps in order to not have a rough cross-section on the edge coupler. At the same time, the gap should be as narrow as possible, considering the working distance of the tapered fiber and the diffraction effect. Hence, the gap between the facet of the edge coupler and the cross-section should be less than 12μm. Unfortunately, the error of the dicing machine is ±14μm which is not enough to achieve the narrow gap. After dicing, only 23% of the cell had a proper gap, and the other 77% has an overbroad gap or got damaged because of the error.

2. A sensitive infrared (IR) camera

There was an IR camera in the lab, but it is not sensitive enough to check whether the IR laser goes through the waveguide or not. Checking the light that goes through the waveguide is quite important to adjust the input fiber.

3. The bend waveguide in order to array the two edge couplers paratactically

As mentioned previously, the unwanted light is caught by the output fiber because the diffracted light that is not inserted into the input coupler can go through above the wafer.

To avoid the light not from the waveguide, the output coupler can be placed not in a line as seen in Figure 5.8. The designed mask has a bend waveguide as seen in Figure 4.8, but the diffracted light is still detected by the output fiber. Hence, the input and output couplers can

be arrayed paratactically so that the diffracted light can be ignored. In this case, if the bend loss and the wafer dicing are considered before design a mask, only one side that has the input/output couplers can be polished to be smoother.

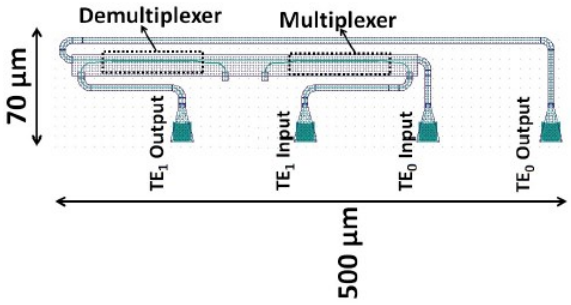

Figure 5.8 The coupler are arrayed paratactically [19], but these are grating couplers. The layout is to explain the array to avoid diffracted light when the edge coupler are used.

4. The design of the heat pads

The designed metal contacts, called the heat pads, can be divided into two parts. One of them is to cover the sensing arm, and the other one is to be contacted by the probe tips. The two parts are connected with the twelve thin bridges as seen in Figure 4.18 and Figure 5.10. There are three major problems which can be solved by designing a better heat pad. The first problem is in the fabrication process. The thin bridges are too thin to get the pattern using the wet etching process. Even if the etch rate was known, it was not easy to get the pattern without over-etching. This is the reason for using the lift-off process to get the heat pads. The second problem is also from the bridges. To flow the current, the wide part of the heat pad is contacted by the probe tips. It was assumed that the current flows through the bridges and the narrow part on the waveguide. However, the current flows mostly into the wide part due to the too narrow bridges. The last problem is contacting. Even though the

wide part was designed to be contacted, it is not wide enough. To solve the three problems, the heat pads and the bridges should be larger, and the part to covering the waveguide can be connected to the two bridges and two wide parts to get current flow above the sensing arm as shown in Figure 5.9.

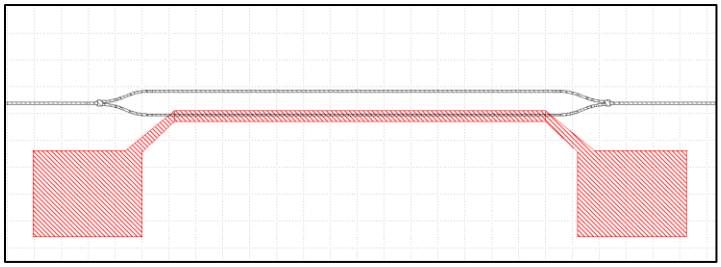

Figure 5.9 The redesigned metal contact (red)

5.3. Heat pads

The metal contact test was performed to check the current flow and the burn-out point. The setup is shown in Figure 5.1, and the probe tips used for this measurement are the tungsten tips (Siganatone, SE-TB). The diameter of the probe tip is 25 μm which is not a small one in the product family, but it can be contacted to the metal contact as seen in Figure 5.10. For the current flow test, the DC power supply and a multimeter were used.

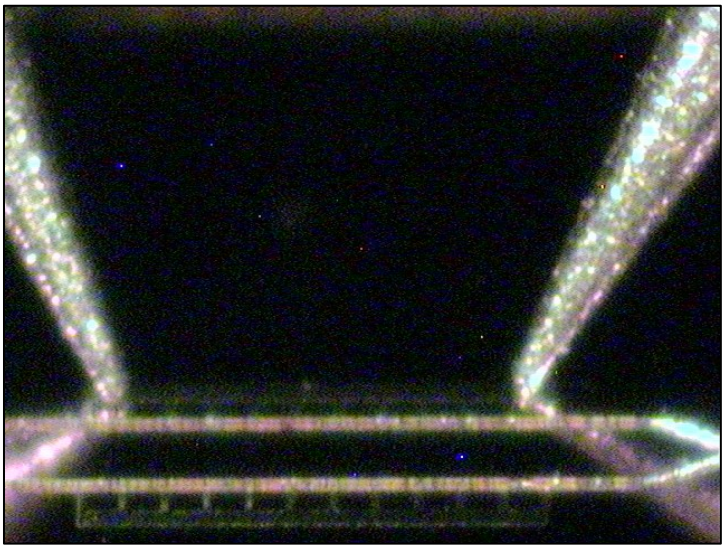

Figure 5.10 Probe tips contacting on the heat pads

As a result of the simulation for the thermo-optic effect shown in Figure 3.16, an electric power of 0.3 W is required to get the Pi phase shift. As a result of the test, the nickel contact is burned at 7~8 volt, and the variation of the current is represented in Table 5.1. A voltage of 5 volts was applied as not to burn the heat pad, and it was enough to bring the Pi phase shift.

Table 5.1 Heat pad test

	Sample 1			Sample 2			
Voltage (V)	Current (A)	Resistivity (Ohm)	Watt (W)	Current (A)	Resistivity (Ohm)	Watt (W)	$\Delta\Phi$
0.5	0.04	11.90	0.02	0.04	13.16	0.02	0.07π
1.0	0.08	12.99	0.08	0.07	13.89	0.07	0.24π
1.5	0.11	13.76	0.16	0.11	14.29	0.16	0.56π
2.0	0.14	13.89	0.29	0.14	14.49	0.28	0.98π
2.5	0.18	13.89	0.45	0.17	14.62	0.43	1.55π
3.0	0.21	14.02	0.64	0.20	14.71	0.61	2.13π
3.5	0.25	14.00	0.88	0.23	15.15	0.81	2.95π
4.0	0.27	14.65	1.09	0.26	15.63	1.02	3.69π
4.5	0.30	15.00	1.35	0.28	15.96	1.27	4.50π
5.0	0.32	15.63	1.60	0.30	16.61	1.51	5.45π

The heat pad test was performed three times per sample, and the results are shown in Figure 5.11. The result shows the stability of the heat pads and the linearity.

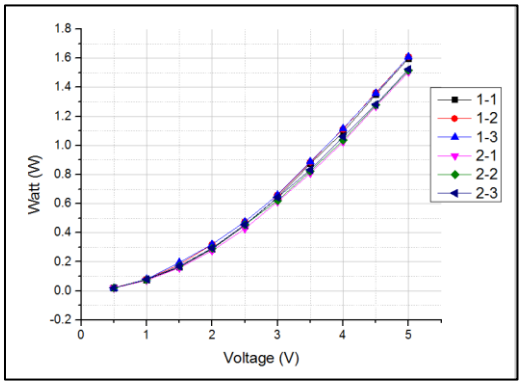

Figure 5.11 Heat pad contact (sample # - test #).

6. Conclusion.

The thermo-optic MZM was designed and fabricated as an active Si photonic device. In this thesis, the design method for each component is described, and the components were simulated by using Lumerical FDTD and Mode solution. Through the simulation result, the dimensions of all the components were decided and drawn by K-layout. The designed masks made by PHOTO SCIENCES were used to fabricate the thermo-optic modulator in the Minds room of RHIT. For the fabrication of the device, a commercial SOI wafer was used, and the thickness of the top silicon layer of the SOI wafer is 2040±80 nm which is thicker than normal because it needs the larger facet of the edge coupler to put the more light in considering the losses of the device.

To fabricate the optical layer, the photoresist AZ5214 was used as a negative PR, and XeF_2 etching system was used to etch the silicon layer. Additionally, to use the photoresist AZ5214 as a negative PR, it requires a flood exposure and a reversible bake. The chemical connection of the photoresist is getting stronger during the additional steps. Hence, it has more residual photoresist on the window than a positive PR. This is the reason for using the HF short time dip to remove the residual organics on the window.

The width of the designed waveguide in the mask is 3.9±0.2 μm and the width of the waveguide after lithography is also 3.9±0.2 μm. However, the width of the waveguide after removing the photoresist is 3.0±0.2 μm due to the isotropic etching. After waveguide patterning, silicon dioxide of 50nm was deposited as a cladding layer to protect the waveguide. To build the metal contacts, lift-off method can be used to omit the etching process. Both processes, the lift-off and the etching, were described in the fabrication

chapter which includes all the details about the process and also failures during experiments.

In the measurement chapter, there is the description of the setup and the test. For the optical test, three different optical fibers were used, and an optical amplifier was connected to the 1553 nm laser diode. So, the optical power from the input tapered fiber can be reached up to the 17.5 dBm (56 mW). However, the fabricated devices are too lossy to transfer the light even though it was amplified and has much more optical power than common optical power (10 mW) in a test. The two main losses are the sidewall lose and insertion loss. The sidewall lose is from the XeF_2 etching, so it needs another etching method and treatment to fabricate a smoother sidewall. KOH etching, which is a wet etching process, can be one method, but it is an anisotropic process. To improve the surface roughness of the waveguide after etching, wet chemical oxidation can be the method. Si waveguide sidewall loss has been reduced from 9.2 to 1.9 dB/cm by the wet oxidation treatment [47]. The second reason for the loss, the insertion loss, is from the wafer dicing. To reduce the insertion loss, the chemical-mechanical polishing and using the milling routers [48] can be methods. The milling routers can minimize the waveguide core end facet RMS roughness to 183 ±13 nm which gives input optical coupling loss of 1.7 ± 0.5 dB.

According to the metal contact test, as shown in Table 5.1, applying the proper electric power for the Pi phase difference has been checked. However, the design of the metal contact can be improved to be more efficient and faster as suggested in Figure 5.9. Furthermore, the layout shown in Figure 5.8 is suggested for the butt coupling to avoid the diffracted light.

For the future work to fabricate the better and faster active devices, the resolution of the fabrication should be decreased. To do this, PECVD machine in Minds room should be studied for the reactive ion etching (RIE) process which is an anisotropic etching method. Secondly, the KOH or TMAH etching instead of the XeF_2 etching can be studied more to create smoother waveguide surfaces.

Lastly, I recommend that future students at Rose-Hulman work with the superior SEM (HITACHI S-3000N) to check the device with the higher resolution and magnification. The challenge of the SEM is that the machine requires a competent user because its autofocus function is not working well. Lastly, installing a sensitive IR camera on the setup would allow the user to measure and check the infrared light going through the waveguide.

REFERENCES

[1] W. N. Ye and Y. Xiong, “Review of silicon photonics: history and recent advances,” *J. Mod. Opt.*, vol. 60, no. 16, pp. 1299–1320, Sep. 2013.

[2] R. Soref, “The Past, Present, and Future of Silicon Photonics,” *IEEE J. Sel. Top. Quantum Electron.*, vol. 12, no. 6, pp. 1678–1687, Nov. 2006.

[3] R. Baets *et al.*, “Integration of photonic functions in and with silicon,” in *Solid-State Device Research Conference, 2004. ESSDERC 2004. Proceeding of the 34th European*, 2004, pp. 57–62.

[4] S. Martin and O. Nert Jan, “Optical Interconnects: Intra-system data transfer with light,” 2005.

[5] “The 50G Silicon Photonics Link.” 2010.

[6] R. Soref and B. Bennett, “Electrooptical effects in silicon,” *IEEE J. Quantum Electron.*, vol. 23, no. 1, pp. 123–129, 1987.

[7] D. C. F. G, M. M, C. G, I. M, R. I, and S. P.M, ““Modulation speed improvement in a Fabry-Perot thermo-optical modulator through a driving signal optimization technique.” 2009.

[8] L. Cao, *High Efficiency Silicon Photonic Interconnects*. Rochester Institute of Technology, 2014.

[9] R. Gautam and others, “Silicon microring resonator loaded mach-zehnder interferometer for low power optical modulation, switching and bio-sensing,” 2014.

[10] “Czochralski process,” *Wikipedia*. 26-Jan-2017.

[11] “Silicon on insulator,” *Wikipedia*. 21-Apr-2017.

[12] “SEH America - SOI Wafer.” [Online]. Available: http://www.sehamerica.com/section.cfm?wSectionID=4834. [Accessed: 10-Sep-2017].

[13] B. Gorka, “Hydrogen passivation of polycrystalline Si thin film solar cells,” HZB, 2010.

[14] L. Ling, “Low Loss Polysilicon Waveguides for Silicon Photonics,” Massachusetts Institute of Technology, 1997.

[15] D. Kwong, A. Hosseini, J. Covey, Y. Zhang, X. Xu, and R. T. Chen, “Low loss polycrystalline silicon waveguides and devices for multilayer on-chip optical interconnects,” 2013, p. 863012.

[16] L. Liao, D. R. Lim, A. M. Agarwal, X. Duan, K. K. Lee, and L. C. Kimerling, “Optical transmission losses in polycrystalline silicon strip waveguides: effects of waveguide dimensions, thermal treatment, hydrogen passivation, and wavelength,” *J. Electron. Mater.*, vol. 29, no. 12, pp. 1380–1386, 2000.

[17] “Total internal reflection,” *Wikipedia*. 08-Jun-2017.

[18] S. Bahaa E.A and T. Malvin Carl, *Fundamentals of Photonics*. Wiley, 2007.

[19] Y. Xiong, “Silicon Photonic Devices for Sensing, Switching, Polarization and Mode Control,” Carleton University Ottawa, 2014.

[20] C. Lukas and H. Michael, *Silicon Photonics Design from devices to systems*. Cambridge University Press, 2015.

[21] C. J. Oton, “Long-Working-Distance Grating Coupler for Integrated Optical Devices,”

IEEE Photonics J., vol. 8, no. 1, pp. 1–8, Feb. 2016.
[22] O. Mitomi, K. Kasaya, and H. Miyazawa, "Design of a single-mode tapered waveguide for low-loss chip-to-fiber coupling," *IEEE J. Quantum Electron.*, vol. 30, no. 8, pp. 1787–1793, 1994.
[23] Y. Fu, T. Ye, W. Tang, and T. Chu, "Efficient adiabatic silicon-on-insulator waveguide taper," *Photonics Res.*, vol. 2, no. 3, p. A41, Jun. 2014.
[24] B. Yu, "Directional Coupler." Yonsei University Lecture note.
[25] L. Cai, R. Kong, Y. Wang, and H. Hu, "Channel waveguides and y-junctions in x-cut single-crystal lithium niobate thin film," *Opt. Express*, vol. 23, no. 22, p. 29211, Nov. 2015.
[26] Y. Zhang *et al.*, "A compact and low loss Y-junction for submicron silicon waveguide," *Opt. Express*, vol. 21, no. 1, pp. 1310–1316, 2013.
[27] Y. Zhang *et al.*, "A compact and low loss Y-junction for submicron silicon waveguide," *Opt. Soc. Am.*, 2013.
[28] "photomask cleaning," *McGill Nanotolls - Microfab*. [Online]. Available: http://mnm.physics.mcgill.ca/content/photomask-cleaning.
[29] "XeF2_tutorial.pdf." .
[30] "Electrical resistivity and conductivity," *Wikipedia*. 07-Jun-2017.
[31] R. A. Mayer, K. H. Jung, W. D. Lee, D.-L. Kwong, and J. C. Campbell, "Thin-film thermo-optic GexSi 1- x Mach–Zehnder interferometer," *Opt. Lett.*, vol. 17, no. 24, pp. 1812–1814, 1992.
[32] "Thermal expansion," *Wikipedia*. 07-Jun-2017.
[33] "Wet Etching Recipes of Metals and Semiconductors." [Online]. Available: http://www.cleanroom.byu.edu/wet_etch.phtml. [Accessed: 13-Jun-2017].
[34] "Silicon," *Wikipedia*. 23-May-2017.
[35] M. Vila, D. Cáceres, and C. Prieto, "Mechanical properties of sputtered silicon nitride thin films," *J. Appl. Phys.*, vol. 94, no. 12, p. 7868, 2003.
[36] F. L, "Semiconductor Basic." [Online]. Available: http://www.iue.tuwien.ac.at/phd/filipovic/node29.html#SECTION00921100000000000000.
[37] "Department of Electrical & Computer Engineering, Brigham Young University," *BYU cleanroom*. [Online]. Available: http://www.cleanroom.byu.edu/semiconductor_properties.phtml.
[38] V. Bhatt and S. Chandra, "Silicon Nitride Films Deposited by RF Sputtering for Microstructure Fabrication in MEMS," *J. Electron. Mater.*, vol. 38, no. 9, pp. 1979–1989, Sep. 2009.
[39] Z. Shiyang, L. G.Q, and K. D.L, "Low-loss amorphous silicon wire waveguide for integrated photonics: effect of fabrication process and the thermal stability," *Opt. Soc. Am.*, 2010.
[40] D. Lysáček and L. Válek, "Structural changes of polycrystalline silicon layers during high temperature annealing."
[41] M. H. Jones and S. H. Jones, "Wet-chemical etching and cleaning of silicon," *Fredericksburg Va Va. Semicond.*, 2003.
[42] B. Inayat, "KOH etching of (100) Si wafer, No1," University of Pennsylvania, 2016.
[43] "Corning OptiFocusTM Collimating Lensed Fiber Product Information." [Online]. Available: http://www.lightwavestore.com/product_datasheet/OFC-FTD-

010C_pdf4.pdf.
[44] "TAPERED AND LENSED FIBERS information." [Online]. Available: http://www.ozoptics.com/ALLNEW_PDF/DTS0080.pdf.
[45] D. Po, "Low loss shallow-ridge silicon waveguide." Optical Society of America, 2010.
[46] K. P. Yap *et al.*, "SOI waveguide fabrication process development using star coupler scattering loss measurements," 2007, p. 680014.
[47] D. K. Sparacin, S. J. Spector, and L. C. Kimerling, "Silicon waveguide sidewall smoothing by wet chemical oxidation," *J. Light. Technol.*, vol. 23, no. 8, pp. 2455–2461, Aug. 2005.
[48] H. Baghsiahi, K. Wang, W. Kandulski, R. C. A. Pitwon, and D. R. Selviah, "Optical Waveguide End Facet Roughness and Optical Coupling Loss," *J. Light. Technol.*, vol. 31, no. 16, pp. 2659–2668, Aug. 2013.

APPENDIX A – Photoresist AZ 5214E Data Sheet

Product Data Sheet

AZ 5214 E

Image Reversal
Photoresist

Clariant

GENERAL INFORMATION

This special photoresist is intended for lift-off-techniques which call for a negative wall profile. Although they are positive photoresists (and may even be used in that way) comprised of a novolak resin and naphthoquinone diazide as photoactive compound (PAC) they are capable of image reversal (IR) resulting in a negative pattern of the mask. In fact AZ 5214E is almost exclusively used in the IR-mode.

The image reversal capability is obtained by a special crosslinking agent in the resist formulation which becomes active at temperatures above 110°C and - what is even more important - only in exposed areas of the resist. The crosslinking agent together with exposed PAC leads to an almost insoluble (in developer) and no longer light sensitive substance, while the unexposed areas still behave like a normal unexposed positive photoresist. After a flood exposure (no mask required) this areas are dissolved in standard developer for positive photoresist, the crosslinked areas remain. The overall result is a negative image of the mask pattern.

As everybody knows a positive photoresist profile has a positive slope of 75 - 85° depending on the process conditions and the performance of the exposure equipment (only submicron-resists get close to 90°). This is mainly due to the absorption of the PAC which attenuates the light when penetrating through the resist layer (so called bulk effect). The result is a higher dissolution rate at the top and a lower rate at the bottom of the resist. When AZ 5214E is processed in the IR-mode this is reversed as higher exposed areas will be crosslinked to a higher degree than those with lower dose, dissolution rates accordingly. The final result will be a negative wall profile ideally suited for lift-off.

The most critical parameter of the IR-process is reversal-bake temperature, once optimised it must be kept constant within ± 1°C to maintain a consistent process. This temperature also has to be optimised individually. In any case it will fall within the range from 115 to 125°C. If IR-temperature is chosen too high (>130°C) the resist will thermally crosslink also in the unexposed areas, giving no pattern. To find out the suitable temperature following procedure is suggested:

Coat and prebake a few substrates with resist. Without exposing them to UV-light subject them to different reversal-bake temperatures, i.e. 115°, 120°, 125° and 130°C. Now apply a flood exposure of > 200mJ/cm² and afterwards immerse them into a standard developer make up, i.e. AZ 351B, 1:4 diluted, or AZ 726 MIF for 1 minute. From a part of the substrates the resist will be removed, another part (those exposed to a too high temperature) will remain with the resist thermally crosslinked on it. Optimum RB-temperature now is 5° to 10°C below the temperature where crosslinking starts.

The flood exposure is absolutely uncritical as long as sufficient energy is applied to make the unexposed areas soluble. 200 mJ/cm² is a good choice, but 150 - 500 mJ/cm² will have no major influence on the performance.

Finally it should be noted that the imagewise exposure energy is lower than with normal positive processes, generally only half of that. So a good rule of thumb is: compared to a standard positive resist process, imagewise exposure dose should be half of that, flood exposure energy double of that for AZ 5214E IR-processing.

Once understanding and being familiar with this IR-procedure it is quite simple to set up a different process for lift-off. A T-shaped profile can be achieved by the following process sequence:

The prebaked AZ 5214E photoresist is flood exposed (no mask) with a small amount of UV energy, just to generate some exposed PAC at the surface. Now the reversal-bake is performed to partially crosslink this top areas. By this treatment a top layer with a lowered dissolution rate compared to the bulk material is generated. After this the resist is treated like a normal positive photoresist (imagewise exposure and development) to generate a positive image! Due to the lower dissolution rate in the top layer a T-shaped profile with overhanging lips will be the result.

PHYSICAL and CHEMICAL PROPERTIES

		AZ 5214E	
Solids content [%]		28.3	
Viscosity [cSt at 25°C]		24.0	
Absorptivity [l/g*cm] at 377nm		0.76	
Solvent	methoxy-propyl acetate (PGMEA)		
Max. water content [%]	0.50		
Spectral sensitivity	310 - 420 nm		
Coating characteristic	striation free		
Filtration [µm absolute]	0.1		

FILM THICKNESS [µm] as FUNCTION of SPIN SPEED (characteristically)

spin speed [rpm]	2000	3000	**4000**	5000	6000
AZ 5214E	1.98	1.62	**1.40**	1.25	1.14

PROCESSING GUIDELINES

Dilution and edge bead removal	AZ EBR Solvent
Prebake	110°C, 50", hotplate
Exposure	broadband and monochromatic h- and i-line
Reversal bake	120°C, 2 min., hotplate (most critical step)
Flood exposure	> 200 mJ/cm² (uncritical)
Development	AZ 351B, 1:4 (tank, spray) or AZ 726 (puddle)
Postbake	120°C, 50s hotplate (optional)
Removal	AZ 100 Remover, conc.

HANDLING ADVISES

Consult the **Material Safety Data Sheets** provided by us or your local agent!
This AZ Photoresists are made up with our patented safer solvent PGMEA. They are **flammable liquids** and should be kept away from oxidants, sparks and open flames.
Protect from light and heat and store in sealed original containers between 0°C and 25°C, exceeding this range to -5°C or +30°C for 24 hours does not adversely affect the properties.
Shelf life is limited and depends on the resist series. The **expiration date** is printed on the label of every bottle below the batch number and coded as **[year/month/day]**.
AZ Photoresists are compatible with most commercially available wafer processing equipment. **Recommended materials** include PTFE, stainless steel and high-density poly-ethylene and -propylene.

APPENDIX B – Photoresist SPR3622 Data Sheet

ROHM and HAAS
ELECTRONIC MATERIALS
MICROELECTRONIC TECHNOLOGIES

MEGAPOSIT™ SPR3600 i-LINE SERIES PHOTORESIST

For Microlithography Applications

DESCRIPTION

MEGAPOSIT SPR3600 i-Line Series Photoresist is a positive photoresist designed for very high-throughout process requirements while still delivering excellent lithographic performance coupled with very good wet etch and thermal stability.

The MEGAPOSIT i-LineSPR3600 Series Photoresist also possesses multi-wavelength capabilities and is an ideal cross over photoresist allowing mix and match capability.

The MEGAPOSIT i-Line SPR3600 Series Photoresist shows good performance on line and space and contact hole applications, it also has a complementary range of L and M dyed products which are ideal for reflective substrates. The dilutions available for SPR3600 allow it to cover resist thickness requirements from 1 µm up to 4 µm allowing a single resist family to meet all the process requirements.

ADVANTAGES

- Extremely high-throughput process—67 mJ/cm² (0.800 µm L/S) and 88 mJ/cm² (0.700 µm CH) i-Line E_s using 30 SSP develop with 0.26N developer at 1.0 µm film thickness
- Flexible develop process allows for maimizing overall throughput by matching exposure and develop process throughput
- Compatible with both 0.24N and 0.26N developers
- g-Line, i-Line and broadband capabilities
- Robust process latitudes
- High thermal (130°C)/etch resistance
- Applications requiring 1.0–4.0 µm film thicknesses
- Recommended for 0.600 µm process design rules and above
- Comprehensive range of L and M dye dilutions also available for reflective substrates

Figure 1. Masking Linearity

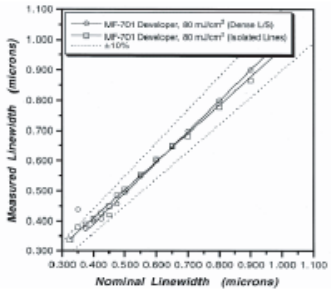

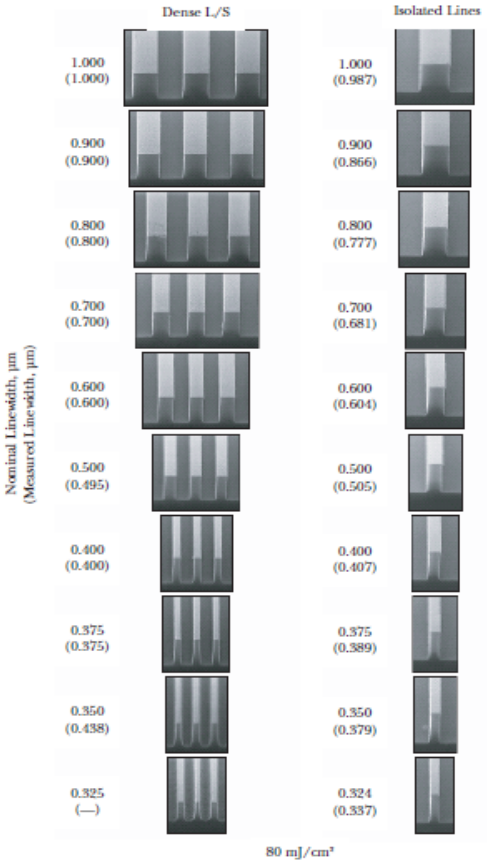

MED6E009, Rev 0
August 2006

2

MEGAPOSIT SPR3600 i-LINE SERIES PHOTORESIST

Figure 2. Exposure Latitude

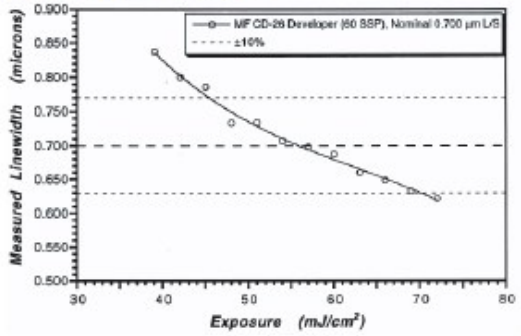

Figure 3. Focus Latitude

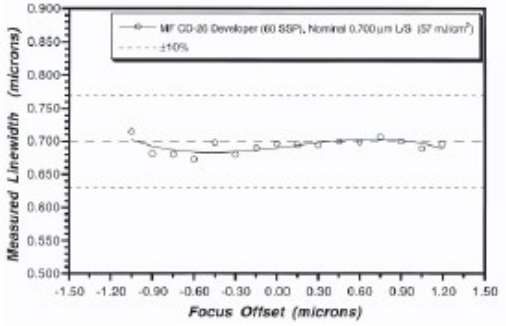

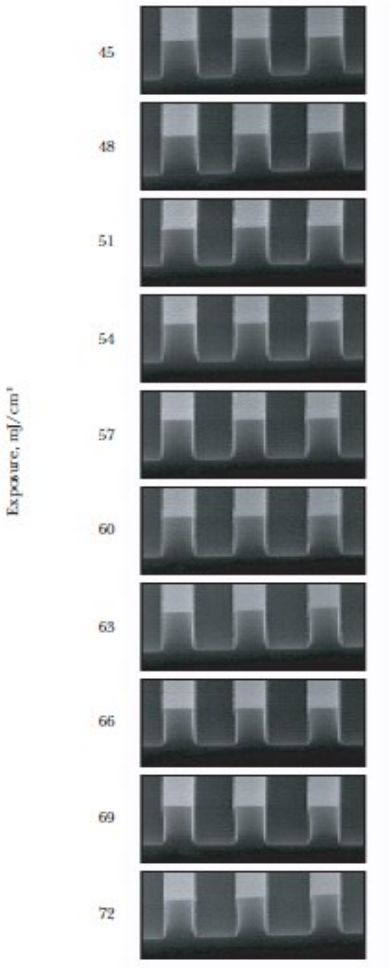

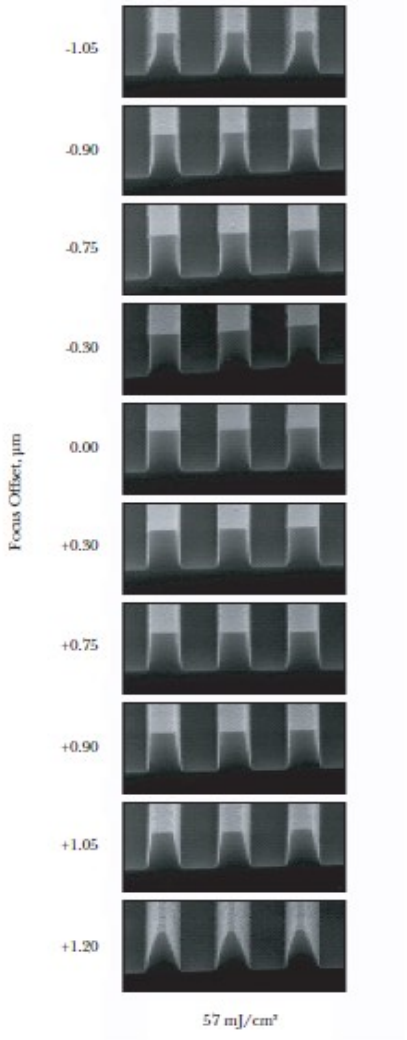

0.700 µm Dense Lines/Spaces	
Sizing Energy (mJ/cm²)	57
%EL (±10% LW)	44.6%

0.700 µm Dense Lines/Spaces	
Depth of Focus (µm) Total (@ Full Film Thickness)	1.95 µm

3

MEGAPOSIT SPR3600 i-LINE SERIES PHOTORESIST

COAT

Figure 4 shows the relationship between spin speed and resist thickness for silicon substrates. Nominal film thickness may vary slightly due to process, equipment and ambient conditions.

Figure 4. Spin Speed Curve

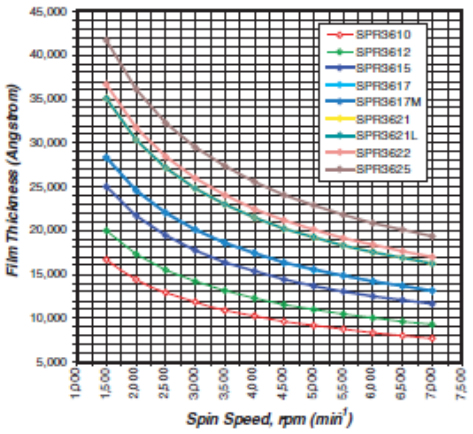

Cauchy Coefficients	
Nx	**SPR3600**
N1	1.611
N2	7.9E + 05
N3	1.3E + 13

Refractive Index	
Wavelength	**n**
365 nm	1.744
436 nm	1.689
633 nm	1.639

SUBSTRATE

SPR3600 is compatible with a wide range of substrates, including but not limited to silicon, SiO_2, polysilicon, nitride and highly reflective metal substrates.

A hexamethyldisilizane (HMDS) based MICROPOSIT™ primer is recommended to promote adhesion with substrates that require such treatment.

Vacuum vapor priming at 120°C for 30 seconds with concentrated HMDS is recommended.

SOFTBAKE

The recommended softbake conditions for SPR3600 are shown in the table below.

Softbake Process Conditions	
Temperature	90°
Time	90 sec. Proximity Hotplate (150 µm) 60 sec. Contact Hotplate

EXPOSE

SPR3600 is sensitive to both g-Line and i-Line exposure wavelengths and can be used as a multi-wavelength crossover photoresist ideal for consolidating processes and reducing the number of photoresists used. The standing wave curve on silicon is shown.

Dill Parameters—365 nm	
	SPR3600
Dill A	0.8100
Dill B	0.0450

Dill Parameters—436 nm	
	SPR3600
Dill A	0.4930
Dill B	0.0480

DEVELOP

SPR3600 is optimized for use with both 0.24N and 0.26N Developers. A single puddle spray process is recommended for most applications and the time can be tailored between 30–60 seconds to give additional throughput benefits. For resist thicknesses above >18,000Å a double puddle spray process can be used, these can be shorter puddles due to the high throughput nature of SPR3600.

Figure 5. 365 nm Swing Curve on Silicon

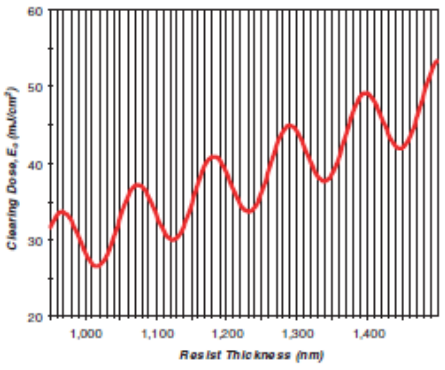

4

MEGAPOSIT SPR3600 i-LINE SERIES PHOTORESIST

POST EXPOSURE BAKE

The recommended Post Exposure Bake (PEB) conditions for SPR3600 on reflective and non-reflective substrates is shown in the table below.

PEB Process Conditions	
Temperature	115°C
Time	90 sec. Proximity Hotplate (150 µm) 60 sec. Contact Hotplate

Figure 6. Thermal Deformation

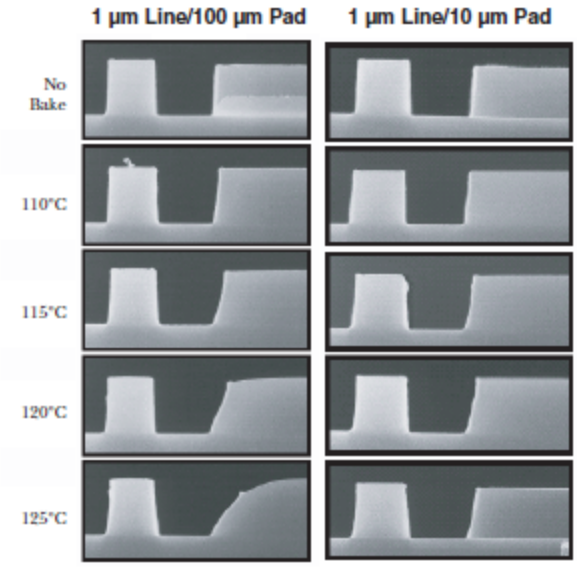

Lithographic Summary—i-Line—10,750Å (E_0 max.) Film Thickness, MF-701 Developer			
Property	**0.700 µm Dense L/S**	**0.700 µm Iso Lines**	**0.800 µm CH**
Photospeed, E_0	47 mJ/cm²	47 mJ/cm²	47 mJ/cm²
Sizing Energy, E_s	83 mJ/cm²	76 mJ/cm²	100 mJ/cm²
E_s/E_0 Ratio	1.77	1.62	2.13
Masking Linearity	0.375 µm	0.325 µm	0.500 µm
Resolution @ E_s	0.350 µm	0.325 µm	0.450 µm
Exposure Latitude	39.8%	43.4%	56.0%
Focus Latitude	1.80 µm	1.80 µm	2.40 µm
Iso/Dense Bias @ E_s	0.018 µm	—	—

Recommended Process Conditions		
	i/g-Line Process	**i/g-Line Process**
Thickness	~10,000–16,000Å	>18,000Å
Softbake	90°C/90 sec. Proximity Hotplate	90°C/90 sec. Proximity Hotplate
PEB	110°C/90 sec. Proximity Hotplate	110°C/90 sec. Proximity Hotplate
Developer	MF CD-26 or MF-26A @ 22°C, 30–60 sec. single puddle	MF CD-26 or MF-26A @ 22°C, 60 sec. double puddle

APPENDIX C –Color chart of silicon dioxide